Ore Geology Reviews 112 (2019) 103024

Contents lists available at ScienceDirect

Ore Geology Reviews

journal homepage: www.elsevier.com/locate/oregeorev

Geology, petrography and mineral chemistry of iron oxide-apatite occurrences (IOA type), western sector of the neoproterozoic Santa Quiteria magmatic arc, Ceará northeast, Brazil

Clóvis Vaz Parente[a,*], César Ulisses Vieira Veríssimo[a], Nilson Francisquini Botelho[b], Roberto Perez Xavier[c], Jacqueline Menez[b], Ramon de Oliveira Lino[d], Cristian Dickson Araújo da Silva[d], Ticiano José Saraiva dos Santos[c]

[a] Universidade Federal do Ceará – Campus do Pici, Bloco 912, 60455-760 Fortaleza, CE, Brazil
[b] Universidade de Brasília – Campus Universitário Darcy Ribeiro, 70910-900 Brasília, DF, Brazil
[c] Instituto de Geociências – Universidade Estadual de Campinas (UNICAMP), Rua Carlos Gomes, 250, Cidade Universitária Zeferino Vaz, 13083-855 Campinas, SP, Brazil
[d] Programa de Pós-Graduação em Geologia da Universidade Federal do Ceará, Campus do Pici, Bloco 912, 60455-760 Fortaleza, CE, Brazil

ARTICLE INFO

Keywords:
IOA deposits
Apatite
Magnetite
Mineral chemistry
Santa Quiteria magmatic arc

ABSTRACT

Iron oxide-apatite (IOA) occurrences have recently been identified in the western sector of the Neoproterozoic Santa Quitéria magmatic arc (Ceará state, northeast Brazil), close to the boundary with the Paleozoic Parnaíba Basin. The IOA mineralization is hosted by albitized metadiorites and metavolcano-sedimentary rocks, which are crosscut by a late- to post-Brasiliano/Pan-African biotite granite intrusion with a U-Pb age approximately 548 ± 4 Ma. Within the metavolcano-sedimentary sequence, metavolcanic rocks are bimodal and consist of albitized metabasalt-andesite and metarhyolites with a U-Pb age of 554 ± 6 Ma, whereas the metasedimentary units are represented by calc-silicate, marble, and pelitic gneisses. The iron oxide-apatite mineralization occurs as (i) banded–stratabound lenses/layers composed of magnetite (50–70%), with or without ilmenite exsolution; apatite (≤8%); monazite; and locally subordinate copper sulfides (~2%); (ii) massive magnetite-(specular hematite)-apatite bodies; (iii) disseminated and vein magnetite-apatite within albitized metadiorite; (iv) massive rhombohedral hematite bodies; and (v) garnet-magnetite type. The host rocks also display marialite, diopside, albite, and epidote (sodic-calcic alteration), biotite and K feldspar (potassic alteration), chlorite and epidote in lower-T hydrothermal alteration assemblages. Mineral chemistry data reveal that (i) except for vein types, apatite in all the other occurrences is F rich (2.4 ≤ F ≤ 4.4%) and low in Cl (< 0.5%), and (ii) magnetite contains variable concentrations of Ti, V, Cr and Ni attributed to both igneous and hydrothermal environments. In addition, the magnetite of the stratabound occurrence is low in TiO_2 (≤1.6%); however, its oxy-exsolutions are rich in TiO_2 (14–52%), indicating a titanium-rich original iron oxide. The low sulfide content and high concentration of apatite indicate that the investigated Fe-P occurrences are of the IOA type, similar to those of IOA provinces elsewhere, such as Kiruna, El Laco, Gushan, Pea Ridge, Pilot Knob, and Bafq. Hence, the discovery of these occurrences in the Neoproterozoic Santa Quitéria magmatic arc has a twofold metallogenic significance: (i) these are the first records of IOA-type deposits in Brazil; and (ii) open a favorability potential for the exploration of IOCG-type deposits in this tectonic domain.

1. Introduction

IOA (iron oxide-apatite) deposits, also known as the Kiruna type, and IOCG (iron oxide-copper-gold) deposits, are part of a set of Fe-rich hydrothermal-magmatic and hydrothermal systems, respectively, of high economic potential; however, they are still controversial in their genesis and classification (Williams et al., 2005; Corriveau, 2007; Groves et al., 2010; Chen, 2013). In the IOCG deposits, the Cu sulfide-Au mineralization, together with a suite of minor elements (e.g., U, Ni, Co, Ag, P, REE, F, Ba), is spatially associated with anomalous concentrations (> 10 vol%) of iron oxides (hematite and/or magnetite) (Hitzman, 2000; Williams et al., 2005). The ore bodies are structurally controlled and associated with a variable combination of extensive and pervasive alkali alteration types, including high-temperature

* Corresponding author.
E-mail address: clovis@ufc.br (C.V. Parente).

https://doi.org/10.1016/j.oregeorev.2019.103024
Received 10 May 2018; Received in revised form 17 June 2019; Accepted 18 July 2019
Available online 25 July 2019
0169-1368/

assemblage represented by albite, diopside, scapolite, magnetite (Na to Ca-Fe alteration) and K feldspar, magnetite (K-Fe alteration), and lower temperature alteration types with assemblages represented by chlorite, sericite, quartz, and carbonate (Skirrow et al., 2007; Corriveau et al., 2016; Montreuil et al., 2016). Genetic models for these systems suppose the mixing of a range of fluid sources: magmatic brines derived from I-type or A-type granitic intrusions, formational/basinal/bittern/evaporitic brines, and meteoric and metamorphic fluids (Barton and Johnson, 1996; Hitzman et al., 1992; Pollard, 2000; Xavier et al., 2008; Chen, 2013; Barton, 2014).

IOA-type deposits form in association with magmatic extrusive to subvolcanic (Frietsch and Perdahl, 1994; Velasco et al., 2016; Tornos et al., 2017) and dioritic intrusions (e.g. Hou et al., 2011). The Fe-P mineralization may occur as massive, tabular or irregularly shaped bodies commonly involved with Na and Na-Ca-Fe alteration types (Williams et al., 2005). Many researchers believe that IOA deposits represent an iron-rich end member or are the deepest parts of larger IOCG system (Hitzman et al., 1992; Barton and Johnson, 2000; Hitzman et al., 2000; Sillitoe, 2003; Mumin et al., 2010; Barton, 2014; Corriveau et al., 2016; Reich et al., 2016). However, the origin of these deposits is also controversial and the following hypotheses have been proposed: (i) magmatic related with the immiscibility process between a Fe, P and volatile-rich magma, which separated from a calc-alkaline to slightly alkaline magma during cooling (Naslund et al., 2002); (ii) hydrothermal involving the transport of Fe by hypersaline fluids at high and low temperatures (Rhodes et al., 1999; Sillitoe and Burrows, 2002); and (iii) hybrid origin involving the combination of the two processes: magnetite-bubble aggregations (Knipping et al., 2015) or volatile-rich iron-oxide melt (Tornos et al., 2016) separated from conjugate silicate melts, which were subsequently overprinted by hydrothermal alteration. The textural and compositional variations in IOA deposits are associated with the timing and depth of the separation of the volatile phase leading to the formation of a complex magmatic-hydrothermal system (Tornos et al., 2017). Among the major deposits of this class are Kiirunavaara, Malmberget, and Grängesberg (Sweden), Mineville (Adirondacks, New York, USA), Pea Ridge (Arkansas, USA), Bafq (Iran), Gushan (China) and El Laco (Chile).

The IOA and IOCG deposits occur in almost all continents. In Brazil, however, investigations of the latter deposit type have been restricted to the Carajás Mineral Province (Monteiro et al., 2008; Xavier et al., 2011; Moreto et al., 2015), whereas the IOA types have not been previously documented until the accomplishment of this work. Here, we present the first report of Fe-P occurrences identified in Brazil, in the western sector of the Neoproterozoic Santa Quiteria magmatic arc (SQMA-Fetter et al., 2003), at the boundary of the Paleozoic Parnaíba Basin, northeast Brazil (Fig. 1). These IOA occurrences are hosted by metadiorites, felsic-mafic metavolcanics, and metasedimentary rocks, which are crosscut by post-Brasiliano/Pan African biotite granite intrusions. The presence of these occurrences in the domain of the SQMA has great metallogenetic significance, since they may have developed in an extensional environment, similar to the Jurassic-Cretaceous deposits of the Chilean and Peruvian iron belts linked to continental-margin, subduction-related magmatic-hydrothermal processes (Treloar and Colley, 1996; Hawkes et al., 2002).

This paper documents the geological, mineralogical and mineral chemistry features related to five IOA occurrences of the SQMA, and it suggests that the origin of these occurrences is likely the result of several ore-forming episodes, ranging from magmatic to hydrothermal.

2. Regional setting

The region of the investigated IOA deposits lies within of supracrustal rocks in the western border of the Neoproterozoic Santa Quitéria magmatic arc (SQMA), a lithotectonic unit located in the northern domain of Borborema Province, northeast Brazil (Fetter, 1999; Fetter et al., 2003). The SQMA consists of an igneous-anatectic complex formed mainly by migmatites (diatexites and metatexites) and granitic rocks with ages between 880 and 460 Ma. The oldest granite rocks (880–800 Ma) represent juvenile arc magmatism; granites dated between 660 and 630 Ma correspond to early-collision granites of a mature arc (Ganade de Araujo et al., 2014); granites aged between 620 and 600 Ma would be the syn-collisional granites or Al-rich anatectic granites, intruded during tectonic thrusting, with the same age as the Brasiliano metamorphism (ca.620 and 600 Ma) (Arthaud et al., 2015); granites aged between 590 and 560 Ma are the late-orogenic granites associated with syn-strike-slip phase (dos Santos et al., 2008) and the younger granites (< 550 Ma) would be the post-orogenic granites (Archanjo et al., 2009; Castro et al., 2012) including the biotite granite dated in this work. Megaenclaves of calc-silicates, marble and amphibolites are common features in this complex (Fetter et al., 2003; Castro, 2004; Arthaud et al., 2008; Costa et al., 2013; Ganade de Araujo et al., 2014). Intermediate metavolcanic rocks (meta-andesites) intercalated with the metasedimentary rocks, as well as skarn deposits of Fe ± Cu, are also present in these arcs, indicating that their lithological association is diversified and has great metallogenetic potential (Parente et al., 2015). The SQMA has a sinuous shape and extends for 220 km towards the NNE-SSW. On both sides, it is bordered by a metasedimentary sequence (quartzite-pelite-carbonate) with intercalations of metabasic rocks which are attributed to the Ceará Complex. This complex is interpreted to have been deposited in a passive continental margin environment around 770 Ma, later evolved to active margin environment during the Neoproterozoic (Braziliano Orogeny), whose regional metamorphism attained its climax at 630–600 Ma (Arthaud, 2007). The rocks adjacent to the arc are marked by metamorphic associations of the high amphibolite to eclogite facies, where the high-grade metamorphic facies are localized next to both borders of the magmatic arc (Garcia and Arthaud, 2004; Castro, 2004; dos Santos et al., 2008; Amaral, 2010). Based on magnetotelluric data, Padilha et al. (2014) confirmed the double convergence subduction indications, in agreement with the petrological data of retroeclogites and high-pressure granulites on both sides of the arc (e.g., Castro, 2004; Garcia and Arthaud, 2004; dos Santos et al., 2008; Amaral, 2010). Padilha et al. (2017) described important magnetotelluric anomalies at the boundary of the Parnaíba Basin with the Precambrian terrains of the Ceará Central Domain (DCC), the site of the main iron occurrences studied in this work and interpreted the boundary as a possible suture zone.

3. Materials and methods

IOA occurrences in the western border of the SQMA were first delimited in the field on the basis of remote sensing image analysis combined with magnetometry and gamma spectrometry during the geological mapping of an area of ca. 300 km^2 between the cities of Ipaporanga and Ararendá. Several mineralized bodies were identified, and five of them were chosen for the study in this work. In this study, petrography was performed on 120 thin sections and 23 polished sections, from which 20 samples were selected for electron probe microanalysis of silicates, iron oxides and apatite. Most of the analyses were performed on the core and rim of the iron oxides and apatite, resulting, respectively, in 76 and 98 reading points. These microanalyses were performed with a JEOL JXA-8230 Electron Probe Microanalyzer (EPMA) at the Institute of Geosciences, Brasília University (IG/UnB). The chemical analyses were obtained using an accelerating voltage of 15 kV, a beam current of 15 nA and a counting time of 10 s; the counting time for backgrounds was always half of the counting time used on the peaks. The X-ray Kα-lines were used for Na, Mg, F, Al, Si, Ca, K, Cl, P, Mn, Ni, Fe, Cr, V, and Ti; the Lα-lines were used for Sr and Ba. The synthetic standards were strontium sulfate (Sr), manganese and titanium oxide (Mn and Ti), nickel oxide (Ni), chrome oxide (Cr) and barite (Ba). The following detection limits were obtained (in wt%): 0.004 for Na, 0.005 for Mg, 0.011 for F, 0.005 for Al, 0.006 for Si, 0.006

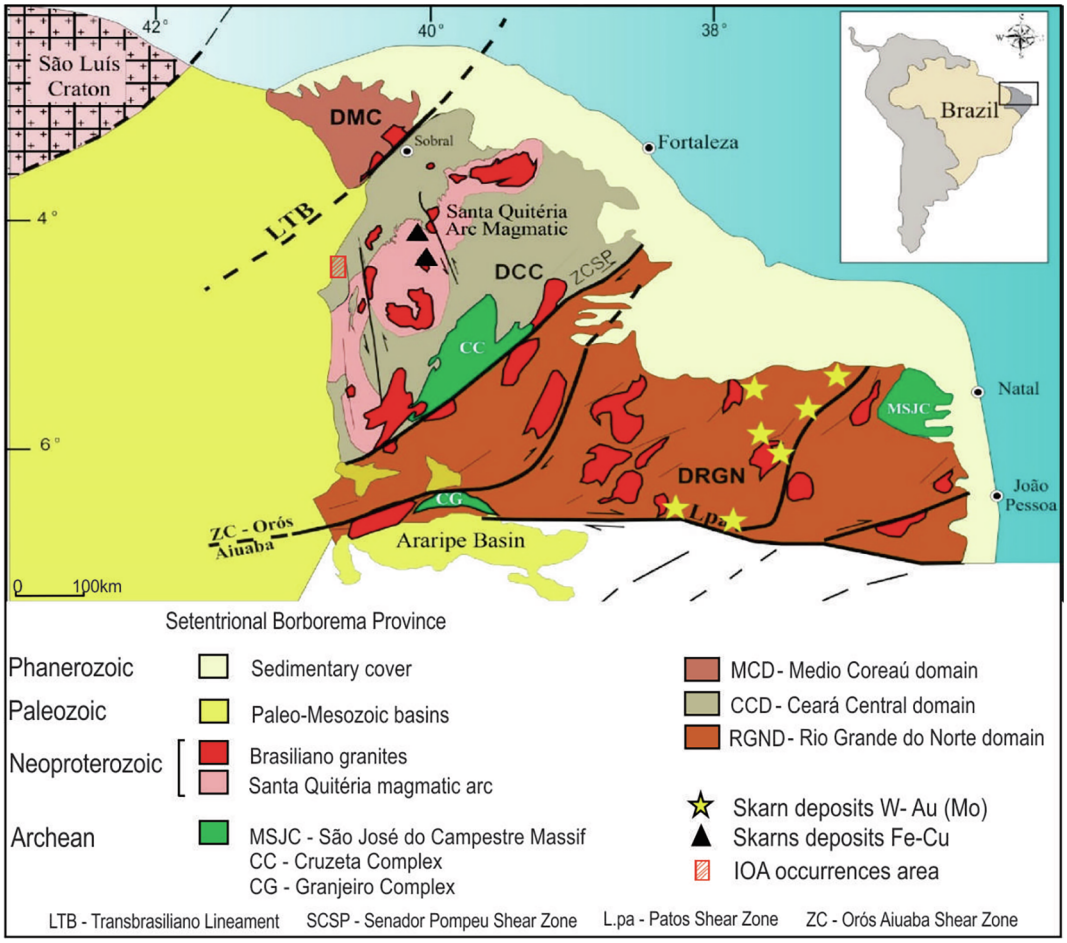

Fig. 1. Simplified geological map of the northern part of Borborema Province with the location of several mineral systems, including the IOA occurrences in the western sector of the Santa Quitéria magmatic arc. Modified from Fetter et al. (2003).

for Ca, 0.005 for K, 0.004 for Cl, 0.007 for P, 0.012 for Sr, 0.016 for Mn, 0.012 for Ni, 0.011 for Fe, 0.009 for Cr, 0.008 for V, 0.010 for Ti, and 0.018 for Ba. U-Pb zircon ages by LA-ICP-MS were obtained in metarhyolite of the Estreito Unit and in intrusive biotite granite that crosscut this unit. The analysis were realized at Isotope Geology Laboratory of Institute of Geosciences (University of Campinas, São Paulo) using a Photon Machines Excite 193 nm, equipped with a two-volume HelEx ablation cell, coupled with an ICP-MS Thermo Fisher Element XR. The laser was pulsed at 10 Hz for 40 s, and fluence commensurate with an approximate pit for the 25 µm diameter spot size analyses. The 91500 zircon (Wiedenbeck et al., 1995) was used as a primary reference material and Peixe zircon (Navarro et al., 2017) was used as quality control reference material. U-Pb data were reduced using Iolite v2.5 Software followed the method described by Paton et al. (2010), which involves subtraction of gas blank followed by downhole fractionation correction comparing with the behavior of the 91500 reference zircon (Wiedenbeck et al., 1995).

4. Geological setting of the investigated IOA occurrences

The main Precambrian lithologic associations of the western boundary SQAM, host or not of the mineralized bodies, occur in the form of blocks and boulders exposed in erosive windows near cliffs and bottoms of valleys formed by the retreat of the Parnaíba Basin sedimentary coverage. Despite the lack of outcrops, the following units are defined, from bottom to top in the area of the IOA occurrences: Ceará Complex, Estreito Unit, late to post-Brazilian granites, Serra Grande Group and Cenozoic cover deposits (Fig. 2A).

The Ceará Complex is a unit of regional expression within the Ceará state and comprises a sequence of amphibolite to eclogite facies sedimentary rocks represented by pelitic gneisses, migmatites, quartzites, marbles, amphibolites, and calc-silicates, (Cavalcante et al., 2003; Arthaud, 2007; Arthaud et al., 2015). Subordinate felsic metavolcanics intercalated within this metasedimentary unit presented U-Pb zircon ages of 749 ± 5 Ma (Arthaud et al., 2015) and 772 ± 31 Ma (Fetter et al., 2003). In the area of the IOA occurrences, this unit is mainly represented by paragneisses, locally migmatized (metatexite/diatexite), marble, and calc-silicate rocks (Fig. 2A, B).

The paragneisses generally appear as loose blocks, and in rare outcrops they exhibit foliation striking N-S and dipping, 35° to W. These rocks are fine- to medium-grained and display compositional/metamorphic banding, with biotite and garnet porphyroblasts, alternating with plagioclase and K-feldspar. The calc-silicates are dark green, medium to coarse-grained rocks, and present often a penetrative tectono-metamorphic foliation and karst features. They are composed of quartz, plagioclase, hornblende, diopside, scapolite and K-feldspar (Fig. 3A).

The Estreito Unit is composed of metavolcanics and hydrothermally altered metadiorites that crosscut the Ceará Complex lithotypes. The metavolcanics, the main host rocks of the stratabound IOA mineralization, are bimodal and represented by metabasalts or metabasalt-andesite and metarhyolites, with irregular or interdigitated contacts suggestive of magma mingling (Fig. 3B, C). This metarhyolite also contains rounded magnetite globules of sizes around 5 mm, disseminated, that indicate contemporaneity between both.

Geochronological data obtained in this metarhyolite yielded a U-Pb

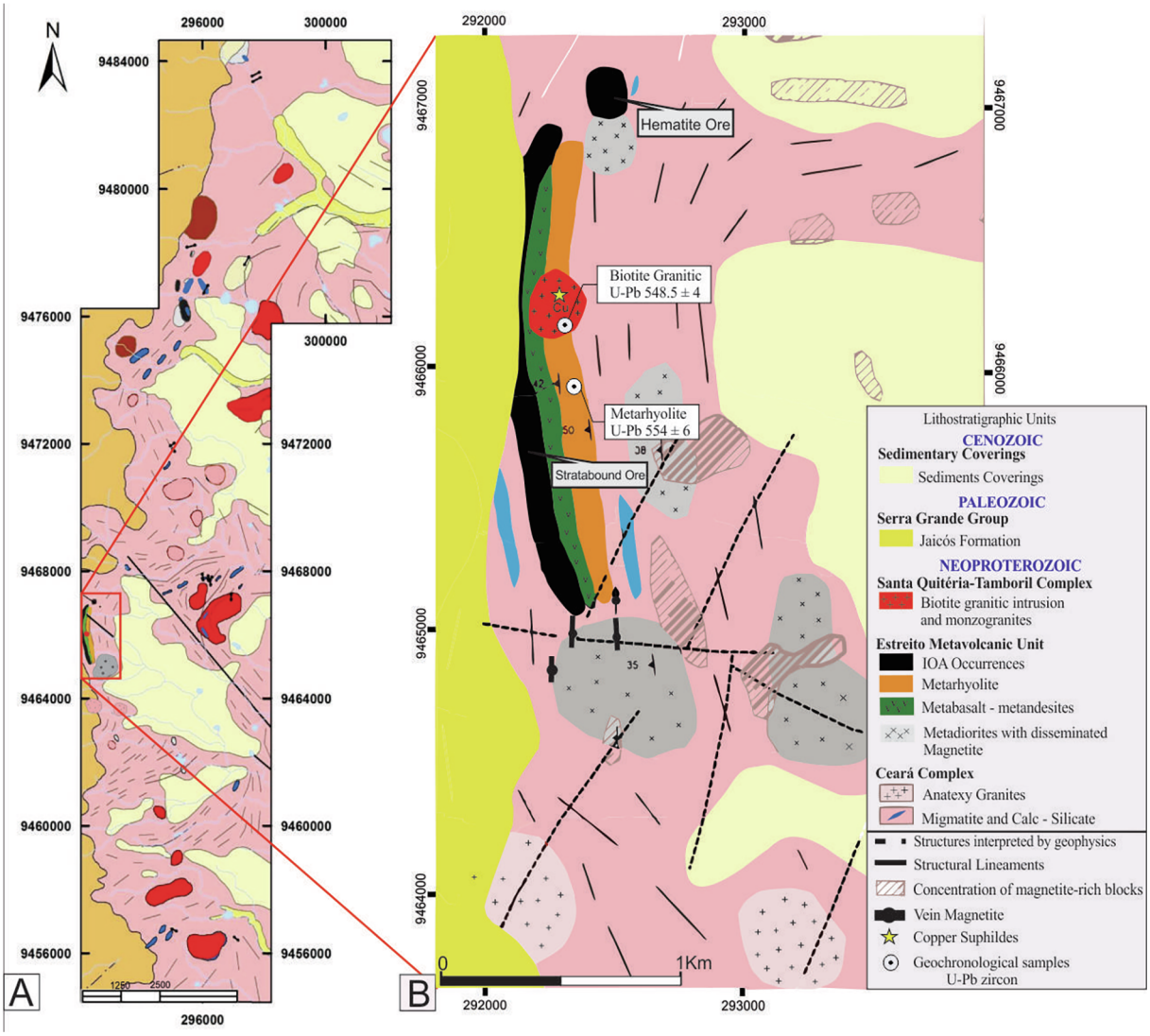

Fig. 2. (A) Geological map of the western sector of the Santa Quitéria magmatic arc displaying the location of the IOA occurrence area investigated in this study. (B) Detailed geological map of the inserted area in A with the location of the main IOA and copper sulfide occurrences.

zircon age of 554 ± 6 Ma (see concordia diagram in item 7.4), which indirectly indicates the age of stratabound mineralization. These host metavolcanics are cut by biotite granite, where they are engulfed in the shape of angular to ovoid xenoliths of various sizes. The metabasalts are composed of a modified mineral assemblage, represented by plagioclase, chloritized amphibole and biotite, and later formed K-feldspar, resulting from potassic alteration. Titanite, ilmenite, magnetite, epidote and apatite appear as accessories. The metarhyolite are porphyritic, with quartz and K-feldspar phenocrysts in a medium crystalline matrix of quartz, plagioclase and alkali feldspar. The volcanic set was subjected to ductile-brittle deformation marked by N-S-striking foliation, dipping 40° to the W, and intrafolial folds oriented along the same direction. The metadiorites occur in the form of blocks, boulders, and slabs in the center-west portion of the area and are the main host rocks of the disseminated and vein IOA mineralization. They are composed of plagioclase, clinopyroxene, amphibole, biotite, magnetite, and quartz. These rocks are commonly affected by albitization, and chlorite alteration (Fig. 3D).

Late to post-Brasiliano granites occur in the form of stocks, dikes, and apophyses. They cut the host rocks and the stratabound mineralization, abruptly and irregularly (Fig. 3E, F). These granites yielded a U-Pb zircon age of 548 ± 3 Ma. They range from gray to pink biotite granite and are slightly deformed. At the contact zone, they are generally hydrothermally altered, marked by microclinization of plagioclase, neoformation of biotite and K-feldspar that exceeds 1 cm in length and by formation of sulfides. The sulfides are represented by chalcopyrite and bornite that are disseminated locally in the stratabound mineralization. In general, the less altered granites are composed of quartz, feldspar, plagioclase, biotite, and muscovite. Epidote, zircon, titanite, and apatite occur as secondary minerals and accessories.

The Serra Grande Group corresponds to the basal unit of the Eopaleozoic Parnaíba Basin and unconformably overlays all lithostratigraphic units mentioned above. It is located in the western portion of the studied area and it consists of beige- to yellow-colored conglomeratic sandstones. This overlying clastic sedimentary unity may have contributed to the preservation of the sulfide mineralization from oxidation and weathering after its formation.

Cenozoic units are characterized by alluvial and colluvial deposits and partially cover the mineralized regions.

5. Iron oxide-apatite occurrences

Five types of Fe-P occurrences have been described in the SQMA. In order of decreasing abundance, they are as follows: (i) banded stratabound magnetite-apatite; (ii) massive magnetite-(specular hematite)-apatite; (iii) disseminated and vein magnetite-apatite; (iv) massive

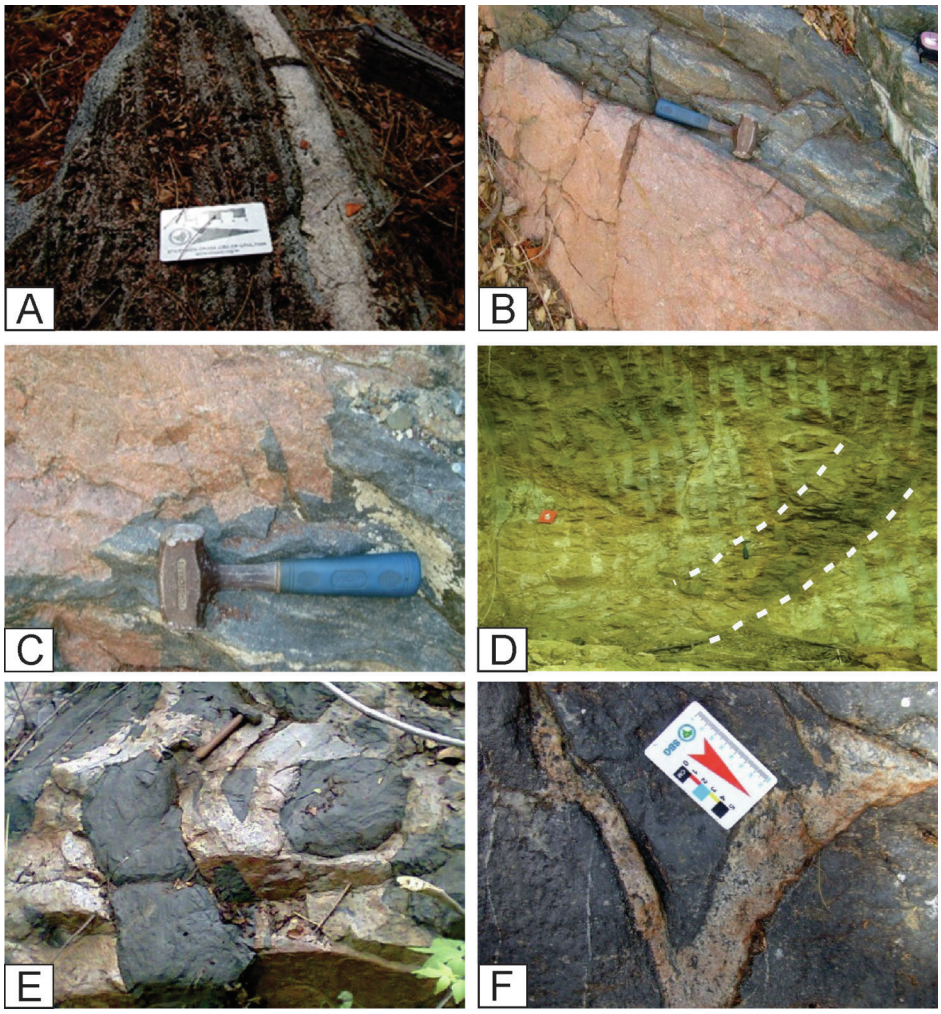

Fig. 3. Host rocks of the IOA occurrences: A. Calc-silicate rocks displaying tectono-metamorphic foliation defined by karstic features; B. Contact of mafic metavolcanic with metarhyolite both are strongly deformed. C. Cuspide contact between mafic metavolcanic and metarhyolite that indicates the coexistence of the felsic and mafic magmas. D. Partially hydrothermally altered metadiorite with magnetite veins, highlighted by the dashed lines. E. Contact of the post-tectonic granite with the stratabound Fe-P mineralization. Note dikes and/or apophyses cutting and embedding this mineralization. F. Irregular granite dike crosscutting the stratabound Fe-P mineralization with the development of neoformed biotite at the interface.

hematite bodies; and (v) a magnetite-garnet type. Table 1 summarizes the main the petrographic features of the mineralizations.

5.1. Banded stratabound magnetite-apatite

This type of occurrence follows the contact of the metavolcanics, where have been subjected to deformation and hydrothermal alteration (Fig. 4A, B). The stratabound mineralization varies from fine-grained (< 1 mm) disseminated magnetite (≤15% magnetite), close to contact with the metarhyolites to coarse-grained (2–3 mm) magnetite in outer zone (Fig. 4C, D). The latter is richer in magnetite (50–70%) (Fig. 4E, F) which typically contain ilmenite oxy-exsolution (Fig. 4G, H). Apatite (≤4%), monazite and subordinate copper sulfides (~1%) are accessories. Apatite crystals are coarse-grained and exhibit subhedral to oval forms as well as recrystallization around its rims, given by the neoformation polygonal grains with angles of 120° (Fig. 5A). Monazite crystals are fine-grained and anhedral and occur at apatite grain edges and in cracks within apatites (Fig. 5B).

The stratabound magnetite-apatite mineralization is cut by a post-Brazilian biotite granite. At the contact zone, granite dikes and apophyses contain massive ovoid to angular xenoliths of the stratabound mineralization (Fig. 5C). Magnetite and apatite are metamorphosed marked by a granoblastic polygonal texture, related to contact metamorphism (Fig. 5D, E). Neoformed biotite of up to 1.5 cm and copper sulfides are also common (Fig. 5F). The sulfide concentration is low and includes chalcopyrite (~3%), bornite (~1%), partly altered limonite and/or goethite (~5%), as well as copper carbonate (~1%) (Fig. 5G). Chalcopyrite grains dominantly occupy the interstices of the magnetite grains and exhibit sizes varying from 0.5 up to 1 mm. Bornite is rare and occurs as inclusions in chalcopyrite with or without lamellae of chalcopyrite exsolution (Fig. 5H).

5.2. Fine-grained massive magnetite-(specular hematite)-apatite

This occurrence type is mainly hosted by paragneiss and calc-silicate rocks (Fig. 6A), and commonly shows cavities that resemble vesicles formed by the escape of volatiles, a primary feature of volcanic rocks (Fig. 6B). It consists essentially of magnetite (~60%), apatite (≤30%) and accessory clinopyroxene. Magnetite is disseminated in aggregates (Fig. 6C) varying between 50 μm and 1 mm in size. Some magnetite crystals have a globule shape with texture variations characterized by anhedral microcrystals in the center, and passing to subhedral aggregates at the edges (Fig. 6D, E). The apatite is euhedral to subhedral, with elongated hexagonal shapes and well-defined faces, some of which contain clinopyroxene inclusions (Fig. 6F). Clinopyroxene is a subordinate phase that occurs in two generations: the first as subhedral crystals, pseudomorphosed by iron hydroxide (Fig. 6E), and the second is represented by aegirine in radial or non-prismatic aggregates occupying part of the matrix. Part of this occurrence also contains specular hematite up to 1 cm among a matrix composed of actinolite, epidote, quartz, and apatite (Fig. 7A). In these blocks, subhedral magnetite is strongly oxidized, sometimes zoned and rimmed by apatite, outlining growth zones (Fig. 7B). The specular hematite crosscuts all other mineral phases of the matrix (Fig. 7C, D). Apatite also occurs in subhedral, hexagonal crystals dispersed throughout the matrix.

Table 1
Synthesis of the main petrographic features of each type of mineralization.

Mineralization type	Ore mineralogy %	Minor Rock-Forming Minerals %	Ore Description	Texture/Characteristics
Fe-P stratabound	Magnetite 50–70, Apatite ≤ 4	Biotite, chlorite, albite, K-feldspar, monazite < 0.1, chalcopyrite < 0.5, bornite < 0.1, chalcocite < 0.5, malachite < 0.1, iron hidroxides < 0.5	Magnetite and apatite crystals are coarse-grained and exhibit subhedral to oval shape as well as recrystallization around its rims, given by the neoformation polygonal grains with angles of 120°. Monazite crystals are fine-grained and anhedral and occur at the edges and in cracks of apatites	Magnetite usually presents ilmenite oxy-exsolution. Magnetite and apatite are recrystallized and marked by a cluster of neoformed crystals with polygonal granular texture, and contacts in triple junctions. The sulfides are interstitials
Fine-grained massive magnetite (-specular hematite)-apatite	Magnetite ~60, apatite ≤30, Hematite ≤ 5	Aegirine-augite, Actinolite, Quartz	Magnetite and apatite are disseminated and in aggregates. Specular hematite is presents in hydrothermalized portions	Shows cavities that resemble vesicles formed by the escape of volatiles. Some magnetite crystals have the globule shape with texture zonations, formed by microcrystals in the center, passing to subhedral aggregates at the edges
Disseminated and vein magnetite in albitized metadiorite	Magnetite 5–80, Apatite < 1	Diopside, actinolite, cummingtonite, albite, chlorite, epidote	Magnetite with lower content is disseminated, and the highest content in veins.	Substitution texture as caries and cuspide texture marked by relicts of clinopyroxene involved by magnetite
Massive hematite bodies	Hematite 95, magnetite ~2	Apatite < 1, gorceixite < 1	Hematite is subhedral to euhedral, and often presents polysynthetic twinning. Magnetite occurs as xenocrystal, marked by irregular microfractures, with sharp and/or lobed contact with hematite.	Hematite with polygonal granular texture, marked by triple junctions with 120° interfacial (or dihedral) angles are common
Magnetite-garnet type	Magnetite ~40	Garnet, diopside, actinolite, quartz	Magnetite occurs in anhedral small crystals, partially martitized, and in the subhedral shape with polygonal contacts, with dihedral limits of 120°, but apparently separated by goethite or limonite films.	Magnetite in subhedral shape exhibits polygonal granoblastic texture.

5.3. Disseminated and vein magnetite in albitized metadiorite

In these occurrence types, the disseminated magnetite (5–20%) occurs locally as aggregates with an annealing texture (Fig. 8A), in a matrix composed of albitized plagioclase and clinopyroxene. The pyroxene crystals are rare and present a carie texture, marked by replacement of magnetite and albitized plagioclase (Fig. 8B). The veins of magnetite occur isolated or in sets that fill N-S-striking *en echelon* fractures with a thickness in the range of 10 cm up to 3 m (Fig. 8C). They are composed of magnetite (~80%), with relicts of clinopyroxene in a carie texture, replaced partially by iron amphibole (~4%) (Fig. 8D, E). In these veins, the magnetite crystals have a polygonal granular texture and are partially martitized (Fig. 8F). Epidote, chlorite, and albite also occur as secondary minerals throughout the host metadiorites. The textural relationship between clinopyroxene and magnetite suggests that the replacement of clinopyroxene by magnetite occurred in a late-magmatic stage, linked to high-temperature magmatic fluids.

5.4. Massive hematite

This occurrence type generally forms topographic highs in the region where it occupies an area of 18,000 m^2 (Fig. 9A). It consists predominantly of rhombohedral hematite (~95%), with a polygonal granular texture, with magnetite (~2%), apatite and gorceixite ($BaAl_3(PO_4)(PO_3OH)(OH)_6$) as accessories. Quartz veins associated with hematite are locally found (Fig. 9B). Magnetite occurs as megacrystals, marked by irregular microfractures, with sharp and/or lobed contacts with twinned or rhombohedral hematite, suggestive of disequilibrium or a substitution texture (Fig. 9C, D). Hematite is subhedral to euhedral, sized between 0.5 and 3 mm and often contains polysynthetic twinning. It exhibits a polygonal granular texture, marked by triple junctions with 120° interfacial (or dihedral) angles (Fig. 9E). The accessory minerals, apatite and gorceixite, present euhedral and anhedral forms, respectively, with the latter, indicated to be the result of apatite alteration (Fig. 9F).

5.5. Magnetite-garnet

This occurrence consists of magnetite (40%) and garnet (35%), with subordinate clinopyroxene, quartz, amphibole, epidote and chlorite, where the latter three are attributed to a retrograde alteration phase (Fig. 10A, B). Magnetite occurs in two generations. The first forms small crystals, partially martitized, surrounded by amphibole (Fig. 10C). The last occurs in the subhedral form with polygonal contacts, with dihedral limits of 120°, but apparently separated by goethite or limonite films (Fig. 10D). These rocks occur as loose blocks next to the contact between metadiorite and calc-silicate rocks, which must imply a genetic link between the two, being able to be interpreted as skarn type occurrences (e.g, Meinert et al., 2005).

6. Hydrothermal alteration

The following hydrothermal alteration types are associated with the Fe-P occurrences: (i) Ca-Na to Ca-Na-Fe; (ii) K-Fe and K-Bt; and (iii) Chl-Ep-Qz. These alteration types vary according to the nature of the host rocks.

In calc-silicate and metavolcanic rocks, Ca-Na alteration is pervasive. It is marked by the formation of scapolite, diopside, albite, and epidote (Fig. 11A) in the calc-silicate rocks, and by clear albite plagioclase, which replaces primary, turbid and altered, plagioclase. It is accompanied by chloritization of the ferromagnesian minerals (Fig. 11B).

In the banded stratabound magnetite-apatite occurrences, the main alteration is a potassic alteration that is localized and developed next to contact of the post-Brazilian biotite granite. This alteration is marked by neoformed K-feldspar and biotite, followed by a phase of copper-rich

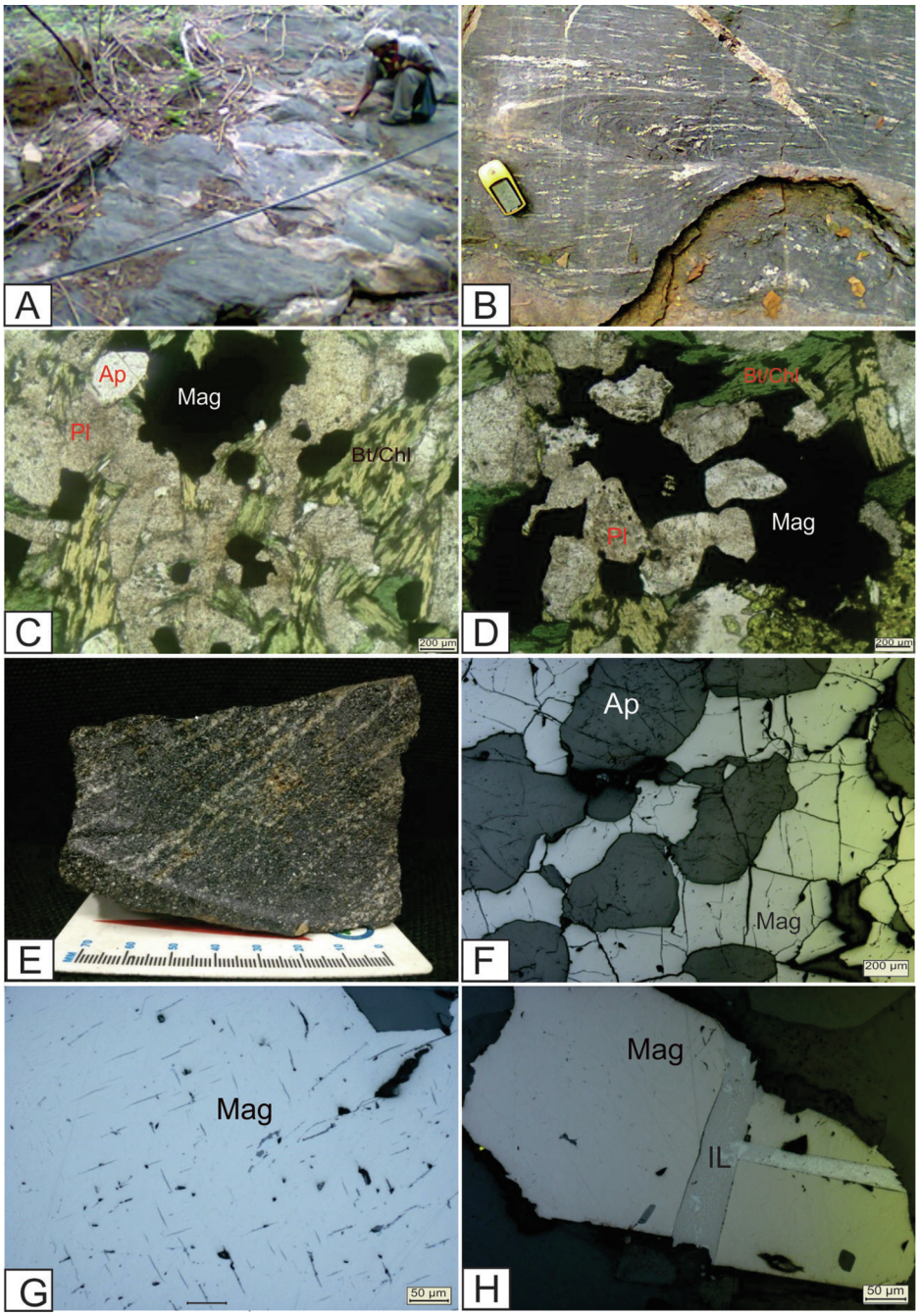

Fig. 4. Styles of mineralization of the SQMA Fe-P occurrences. A. Stratabound Fe-P mineralization cut by dikes and/or apophyses of granitic rocks. B. Stratabound Fe-P mineralization exhibiting features of deformation post-mineralization as intrafolial folds and small biotite granite dyke. C. Photomicrograph of metabasalt-andesite (transmitted light PPL) showing amphibole, chloritized biotite and turbid plagioclase containing magnetite and disseminated apatite. D. Photomicrography of metabasalt-andesite (transmitted light, PPL) showing a higher concentration of magnetite with early plagioclase enveloped by later magnetite. E. Medium-granulated stratabound ore with slightly banded structure post-mineralization. F. Photomicrograph (reflected light, PPL) showing the detail of a microband marked by the alternation of magnetite and apatite. G. Photomicrograph (reflected light, PPL) displaying trellis-type ilmenite lamellae in magnetite. H. Photomicrograph (reflected light, PPL) with sandwich intergrowth of ilmenite lamellae in magnetite. Note that the ilmenite exsolution is oxidizing to hematite, suggesting a later stage of interaction with a strongly oxidizing solution. Abbreviations: Ap-apatite; Mag-magnetite; Bt/Chl-chloritized biotite; Pl-plagioclase; Il-ilmenite.

sulfidation (Fig. 11C, D).

In the fine-grained massive magnetite-(specular hematite)-apatite occurrence, there is an enrichment in Na, Fe, Si, halogen and H_2O represented by the formation of aegirine in fiber-radial aggregates (Fig. 11E), actinolite, hematite, epidote, and quartz in vesicles or amygdala (Fig. 11F). The formation of the aegirine can occur via the following reaction (e.g. Marks et al., 2003):

$$4CaFeSi_2O_6 + 4Na^+ + O_2 + 2H_2O \rightarrow\!\!\!\!\!- \gg 4NaFeSi_2O_6 + 4Ca^{2+} + 4OH^-$$

Augite — Aegirine

The released Ca tends to form Fe-rich Ca-silicates, such as Fe-actinolite and epidote, which are present in the magnetite-(hematite)-apatite occurrences. Alteration in the metadiorite, host of the disseminated and vein mineralization types, is marked by a pervasive high-temperature Na to Ca-Fe assemblage composed by diopside, albite, disseminated magnetite, and, subordinately, garnet, similar to those found in endoskarn (Fig. 12A). The high-temperature assemblage is overprinted by a low-temperature assemblage composed of chlorite, albite, and epidote. The latter occur as pervasive and infill texture in irregular or *en echelon* microfractures in the magnetite (Fig. 12B and C).

In magnetite-garnet occurrences, the clinopyroxene-garnet-magnetite assemblage is the product of the Ca-Na-Fe alteration resulting from an early high-temperature prograde reaction between calc-silicate and metadiorite rocks, while amphibole, epidote, and chlorite are associated with a retrograde alteration phase. Table 2 synthesizes these features.

7. Analytical results

7.1. Mineral chemistry

Microprobe chemical analyses were carried out on apatite and

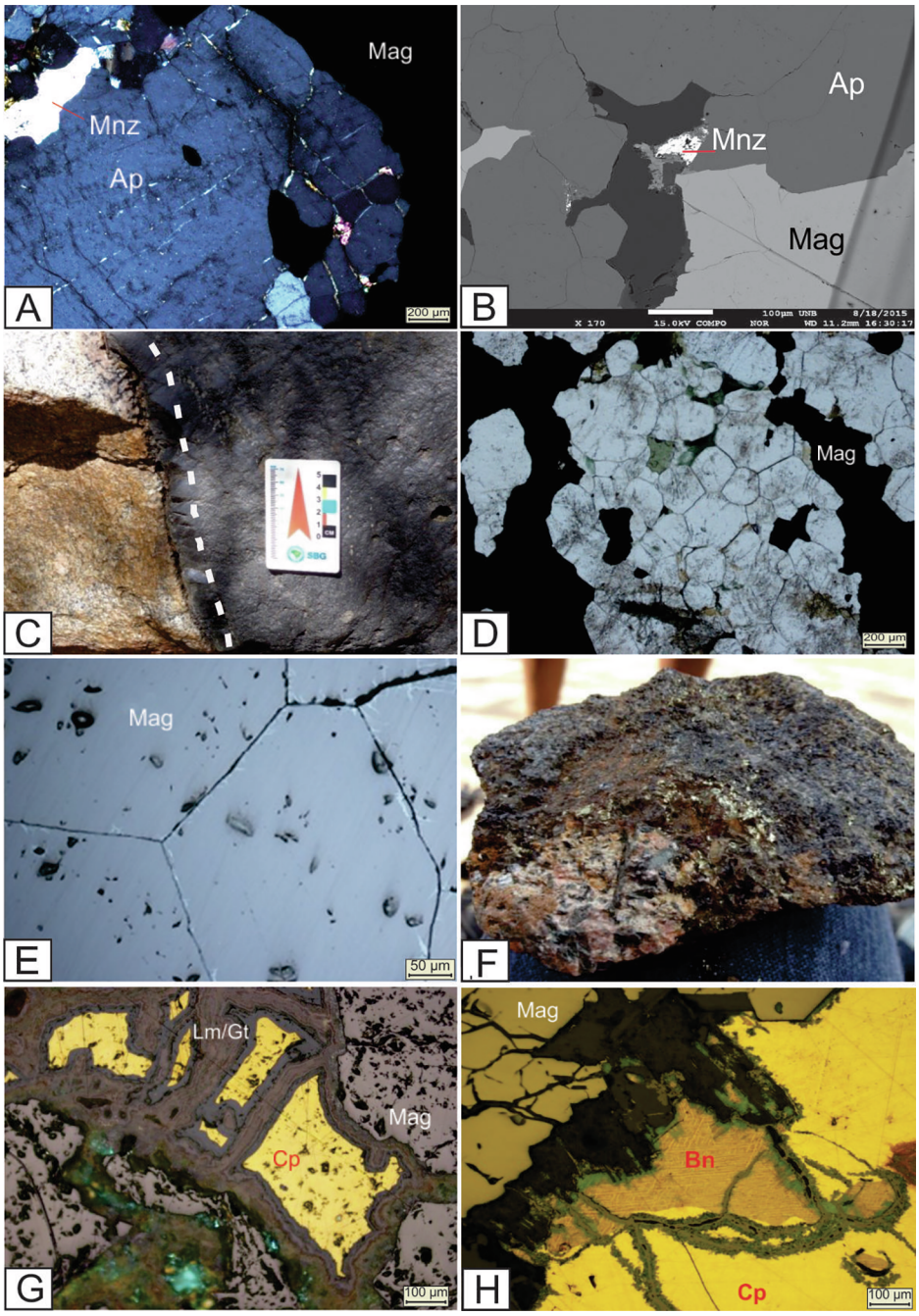

Fig. 5. A. Photomicrograph (transmitted light, PPL) showing an apatite crystal with recrystallization along its rim marked by small polygonal grains. B. SEM-BSE image of monazite in micro fractures in apatites. C. Sharp contact of the biotite granite with the stratabound Fe-P mineralization. D. Photomicrograph (transmitted light, PPL) of apatite aggregates with polygonal granoblastic texture in association with magnetite, as a result of contact metamorphism. E. Photomicrograph (reflected light) showing a detail of polygonal texture in magnetite aggregates in the contact zone. F. Biotite granite (pink color) in sharp contact with the stratabound Fe-P mineralization. Note the contact is marked by the neoformation of the biotite of up to 1.5 cm and concentrations of copper sulfides. G. Photomicrograph (reflected light, PPL) of the Fe-P mineralization exhibiting anhedral chalcopyrite crystals occupying the interstices of the magnetite grains, being partially replaced by goethite/limonite and malachite. H. Photomicrograph (reflected light, PPL) with an anhedral crystal of bornite included in chalcopyrite, both with irregular microfractures filled with chalcocite. Note also tiny chalcopyrite exsolution in the bornite. Abbreviations: Mnz-monazite; Cp-chalcopyrite; Bn-bornite; Lm/Gt-limonite/goethite. (For interpretation of the references to color in this figure legend, the reader is referred to the web version of this article.)

magnetite from the different types of ore and host rock. Tables 3 and 4 present the mineral chemistry data representative of these minerals. The complete dataset is provided in the Electronic Supplementary Material.

7.2. Apatite

7.2.1. Halogens

The apatite of the stratabound mineralization has high contents of fluorine (2.4 ≤ F ≤ 4.4%), low contents of Cl (0.03 ≤ Cl ≤ 0.5%), and OH in the 0.3–7.8% range, being classified as fluorapatite (F > Cl or OH) and/or hydroxyapatite (OH > Cl or F). The massive hematite-type apatite also contains high values of F (3.0 ≤ F ≤ 4.6%), and low Cl (≤0.2%) and OH, varying from 0 to 5.67%. Apatite in metadiorites and metabasalt-andesites are also classified as fluorapatite. The former contains 2.8 ≤ F ≤ 4.1%, 0.04 ≤ Cl ≤ 0.07%, and 0.6 ≤ OH ≤ 1.57%, whereas the latter exhibits 3.1 ≤ F ≤ 4.7%, 0.01 ≤ Cl ≤ 0.03%), and OH (2.5 ≤ OH ≤ 4.2%). The vein apatite, however, has the lowest F contents (F ≤ 0.33%), and the highest levels of Cl (1.92–2.89%), while OH is low (0.16–0.61%), which places them as chlorapatite (Cl > F or OH). A single magnetite-garnet apatite analysis revealed a high content of F (6.5%), low content of Cl (0.01%), and OH at 1.9%. These data are shown in the diagrams F-Cl-OH and F vs Cl below (Fig. 13A, B), and indicate a wide dispersion of the F-Cl-OH anions. This seems to reflect, in part, analyses performed on different parts of the apatite (edge and center) indicative of variations in fHF and fHCI in the magmatic fluids or mixing of fluids (e.g., magmatic and metamorphic fluids).

7.2.2. Minor and trace elements

The Sr, Y, and Mn concentrations in apatite are also distinct between the different types of Fe-P occurrences. The values of Sr, Y, and Mn of apatite in the stratabound magnetite-apatite occurrences vary

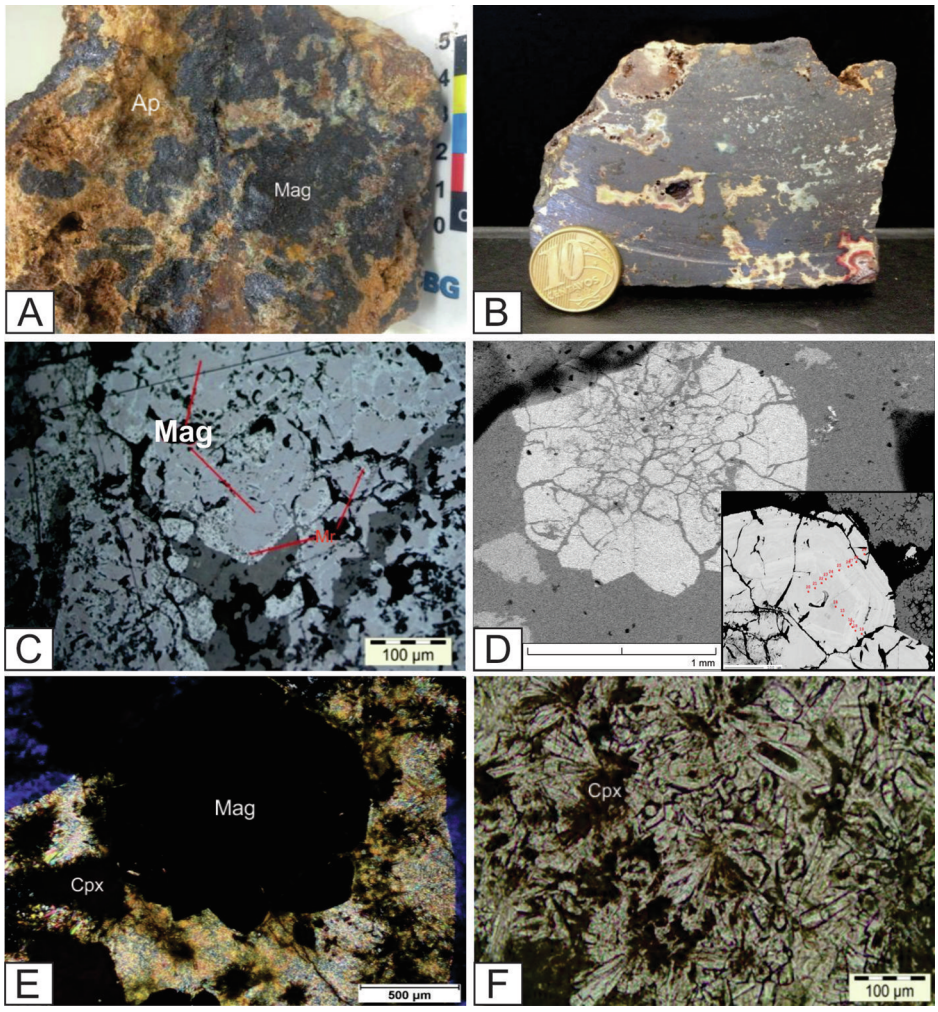

Fig. 6. Fine-grained massive magnetite-apatite mineralization. A. Magnetite sample with irregular portions of apatite (brown) and irregular aggregates of clinopyroxene (blue-green). B. Magnetite sample with volatile escape vesicles, C. Photomicrograph (reflected light, PPL) displaying aggregates of microcrystalline magnetite crystals with partially martitized edges. D. SEM-BSE image of magnetite in globules with textural zoning. Note microcrystals in the center and subhedral aggregates, sometimes zoned, on the edges that are highlighted in detail in the lower corner. This zonation suggests an early microlith and late subhedral magnetite crystallization from volatile-rich iron-oxide melt or fluid. E. Photomicrograph (transmitted light, PPL) with magnetite globules in a matrix composed of fiber-radial aegirine. Note some brownish (oxidized) subhedral crystals in the middle of the matrix, probably augite, which are bordered by fiber-radial crystals of aegirine. F. Photomicrograph (transmitted light, PPL) showing aggregates of euhedral, microcrystalline apatite crystals, some of which have clinopyroxene inclusions. Abbreviations: Ap-apatite; Mag-magnetite; Cpx-clinopyroxene. (For interpretation of the references to color in this figure legend, the reader is referred to the web version of this article.)

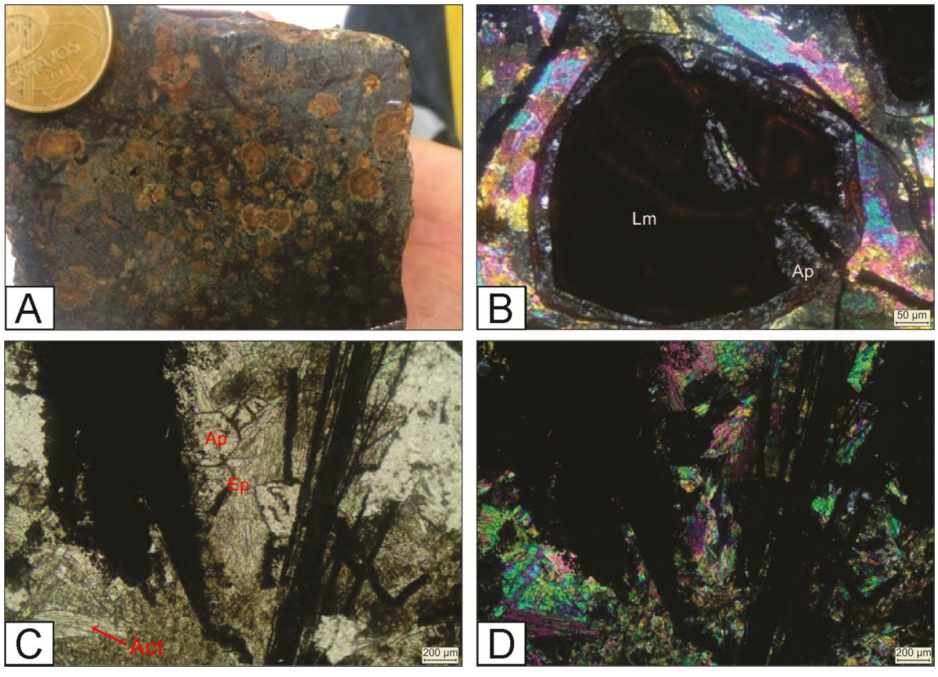

Fig. 7. Fine-grained magnetite-(specular hematite)-apatite mineralization. A. Sample with subhedral iron oxide alteration to limonite, specular hematite in a matrix with ferromagnesian silicates and disseminated apatite. B. Photomicrographs (transmitted light, PPL) with limonitized iron oxide, including apatite, surrounded by an apatite ring, followed by a tiny ring of iron oxide in the middle of the matrix with epidote and actinolite. C and D. Photomicrograph (transmitted light, PPL and cross-polarized transmitted light, XPL) with specular hematite crystals truncating subhedral crystals of apatite, epidote, and actinolite. Abbreviations: Ap-apatite; Mag-magnetite; Lm-limonite; Ep-epidote; Act-actinolite.

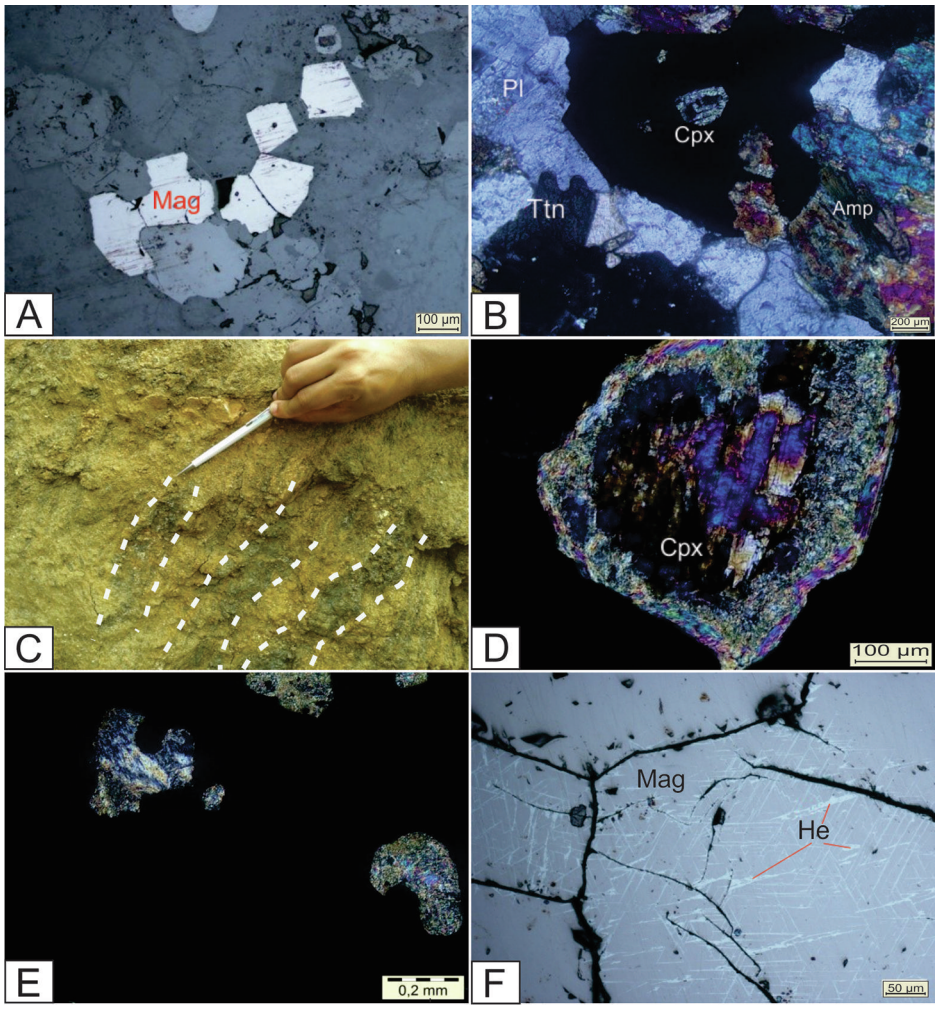

Fig. 8. Disseminated and vein magnetite in albitized metadiorite. A. Photomicrograph (reflected light, PPL) displaying disseminated magnetite with an annealed magnetite texture. B. Photomicrograph (cross-polarized transmitted light, XPL) showing the caries texture given by the replacement of calcic pyroxene by magnetite. C. Small *en échelon* veins of magnetite; D. Photomicrograph (cross-polarized transmitted light, XPL) showing clinopyroxene crystal changed to iron amphibole, both partly replaced by magnetite. E. Photomicrographs (cross-polarized transmitted light, XPL) displaying the cusp and carie texture between magnetite and the pseudomorph of pyroxene. F. Photomicrograph (reflected light, PPL) showing magnetite crystals with polygonal texture and partially martitized. Abbreviations: He-hematite; Cpx-clinopyroxene; Ttn-titanite; Amp-amphibole.

from below the detection limits (bd) to 1706 ppm, 291 to 2331 ppm, and 457 to 4175 ppm, respectively. In apatite of the massive hematite-type, Sr ranges from 481 to 2627 ppm, whereas Y and Mn vary from 220 to 653 ppm and from (bd) to 1069 ppm, respectively. In the disseminated-type mineralization in metadiorite, apatite has no Sr, and Y contents are in the (bd) −134 ppm range, whereas Mn varies from 62 to 294 ppm. In vein apatite, Sr ranges from (bd) to 1267 ppm, Y from 402 to 1205 ppm and Mn from (bd) to 728 ppm. In the host basalt-andesitic, apatite values for Sr, Y, and Mn oscillate between (bd) and 177 ppm, 693 and 1355 ppm, and 124 and 1100 ppm, respectively.

The variations of the apatite trace-element concentrations seem related to the host rock type, which, being of igneous origin, can indicate the degree of fractionation and the oxidation state of the magma—important parameters in mineralizing processes (Belousova et al., 2002). In the Sr versus Y diagram (Fig. 14A) which is related to differentiation indices (from ultramafic to granitic), and decreasing temperature (e.g., Belousova et al., 2002), the apatites of the hematite occurrence present higher and lower concentrations of Sr and Y, respectively, among all others types of mineralizations. In some of the other occurrences (vein, metabasalt-andesitic and metadiorite), the Sr concentration was below the detection limit. Additionally, most of these apatites, mainly the stratabound type, are concentrated in the field of mafic rocks and the Kiruna-type ore. Mn concentration also varies due to the degree the fractionation of the host rocks and its oxidation state (Belousova et al., 2002). Mn^{2+} substitutes for Ca^{2+} and, higher Mn concentration can be associated with apatite developed in more reduced conditions, probably at a level deeper, while the lower Mn contents are in apatite formed in the more oxidizing environments (e.g., Xavier et al., 2011). Therefore, the low Mn concentrations in apatite associated with hematite ore are consistent with the oxidizing conditions needed to form hematite (Fig. 14B).

7.3. Magnetite

7.3.1. Major, minor and trace elements

The magnetite of the stratabound mineralization, shows contents of FeOt from 84.07 to 95.08%, TiO_2 from bd to 1.63%, and V_2O_3 from 0.04 to 0.23%, whereas the ilmenite exsolutions contain FeO, TiO_2, and V_2O_3 in the ranges 19.36–78.68%, 14.20–52.44% and 0.23–0.46%, respectively. The exsolutions represent a titanium-rich original iron oxide, probably a titanomagnetite, which by oxy-exsolution evolved to the intergrowths of pure magnetite and ilmenite, a characteristic feature of magmatic magnetite (e.g., Grant, 1984). Fig. 15 shows a negative correlation between the TiO_2 and FeOt concentrations of the magnetite and ilmenite exsolutions, which reinforces these arguments. In addition, the lower TiO_2 contents are associated with the ilmenite exsolutions in a trellis-type texture, whereas the higher contents are correlated with the sandwich type. Magnetite from the other mineralization types, which has no exsolution of ilmenite, shows ≥89% FeOt and are TiO_2-poor (≤0.9%).

Nadoll et al. (2015) proposed that the concentrations of Ti and V in magnetite can be used to discriminate magnetite from igneous, magmatic-hydrothermal and low-temperature hydrothermal sources (Fig. 16). Titanium concentrations higher than 5000 ppm can be found in igneous magnetite, while low V-Ti concentrations suggest hydrothermal magnetite. Samples of the disseminated magnetite and part of

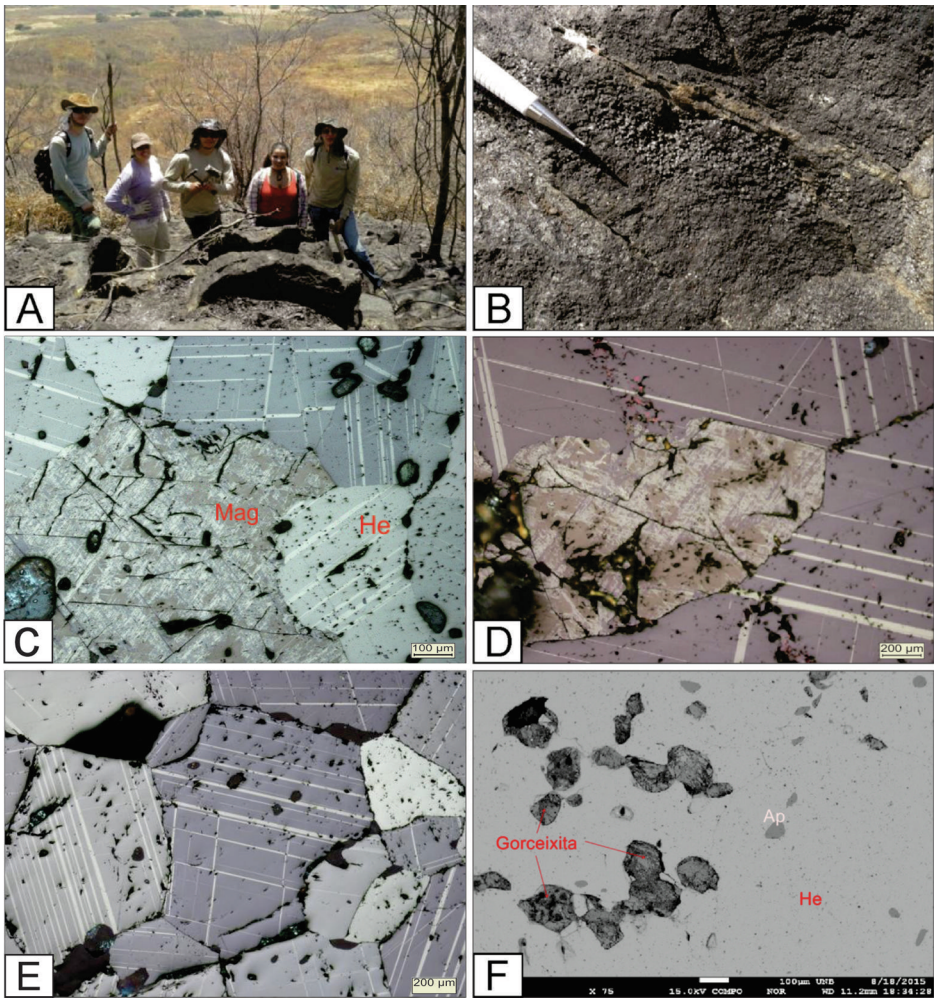

Fig. 9. Massive hematite mineralization. A. View of the hill composed of blocks and boulders of the hematite ore. B. Hematite boulders with quartz veins. Note alongside the quartz veins, the strip with clusters of euhedral hematite probably replacing magnetite. C and D. Photomicrograph (cross-polarized reflected light, XPL) with magnetite megacrystals surrounded by hematite. Note that the magnetite is microfractured and martitized and its fractures do not propagate through the hematite. E. Photomicrograph (cross-polarized reflected light, XPL) with twinned hematite exhibiting polygonal texture. F. Photomicrograph (reflected light, PPL) showing disseminated gorceixite and apatite crystals in hematite mineralization. Abbreviations: Ap-apatite; Mag-magnetite; He-hematite.

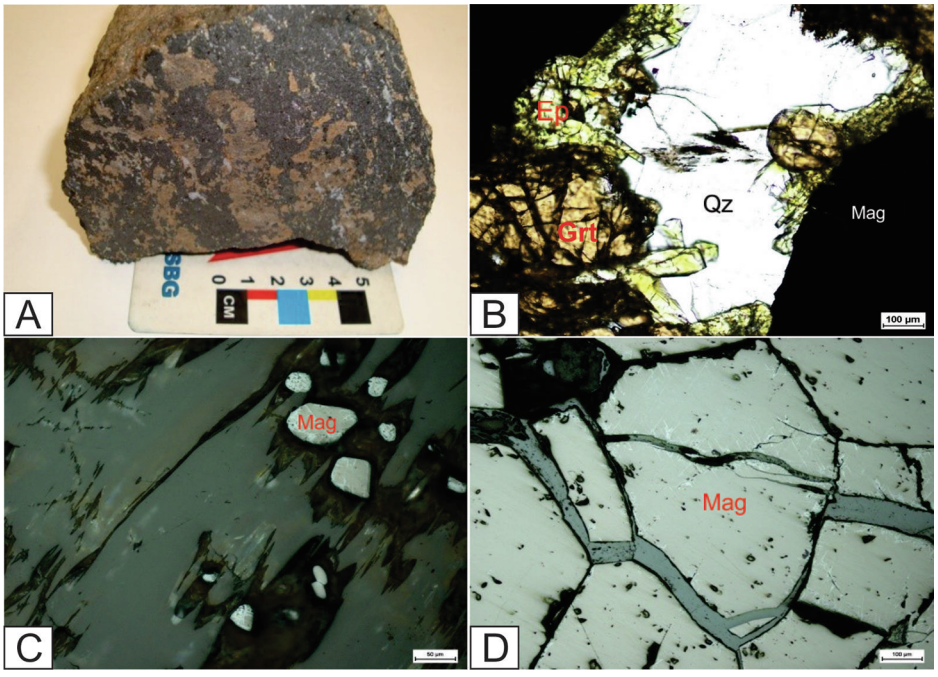

Fig. 10. Examples of garnet-magnetite-type occurrences. A. Sample of a skarn type occurrence, dominated by garnet and magnetite. B. Photomicrograph (cross-polarized transmitted light, XPL) with garnet, magnetite, epidote and quartz. C. Photomicrograph (cross-polarized reflected light, XPL) with small crystals of disseminated magnetite, surrounded by amphibole. D. Photomicrograph (cross-polarized reflected light, XPL) showing aggregates of magnetite crystals exhibiting polygonal granoblastic texture. Some crystals are slightly martitized. Note goethite films at the interface of crystals. Abbreviations: Grt-garnet; Qz-quartz; Ep-epidote.

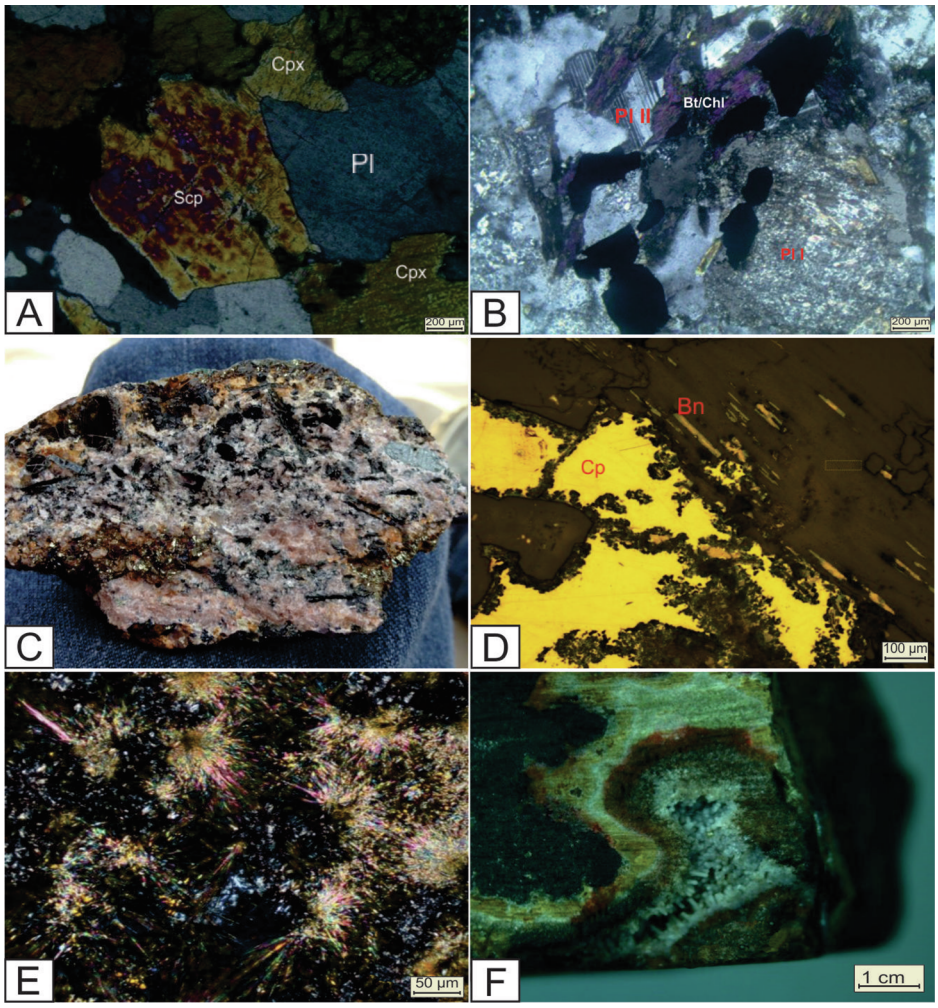

Fig. 11. Hydrothermal alteration assemblage. A. Photomicrograph (cross-polarized transmitted light, XPL) of the calc-silicate rock with a mineral association composed by plagioclase, marialite, and diopside. B. Photomicrograph (transmitted light, XPL) of the metabasalt-andesite exhibiting clear albite replacing the older, turbid and altered plagioclase. Note also the chloritization of ferromagnesian minerals. C. Sample of granite with potassium alteration, marked by neoformation of biotite megacrystals being partially replaced by chalcopyrite and bornite. D. Photomicrograph (reflected light, LPL) of the sulfidation phase with chalcopyrite and bornite replacing the biotite along the planes of cleavage and between silicates. Note also that both sulfides are partly replaced by chalcocite. E. Photomicrograph (transmitted light, XPL) displaying fiber-radial aegirine crystals and microgranular aggregates of apatite. F. Sample with vesicle or amygdala with compositional and textural zonation, marked from the edge to center by aegirine (light green), epidote, iron hydroxide and quartz in the center. Abbreviations: Cpx-clinopyroxene; Scp-scapolite; Pl I-first plagioclase; Pl II-second plagioclase. (For interpretation of the references to color in this figure legend, the reader is referred to the web version of this article.)

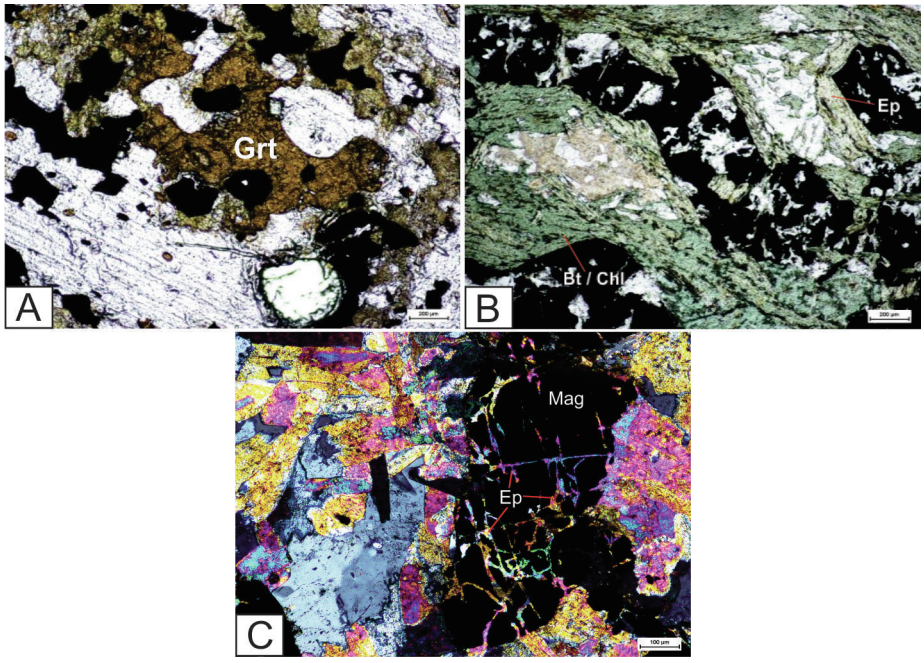

Fig. 12. Hydrothermal alteration assemblage. A. Photomicrograph (transmitted light, LPL) showing garnet, albite, diopside, and epidote in albitized metadiorite. B. Photomicrograph (transmitted light, XPL) exhibiting infill and pervasive alteration. The infill alteration is characterized by epidote in irregular microfractures in magnetite crystals, while pervasive is developed at the dioritic matrix that is strongly altered to epidote and albite. C. Photomicrograph (transmitted light, LPL) exhibiting pervasive alteration characterized by the chloritization of ferromagnesian minerals and albitization of plagioclase. Note *en échelon* microfractures in the magnetite filled by chlorite and albite. Abbreviations: Grt-garnet; Mag-magnetite; Ep-epidote; Bt-chl- chloritized biotite.

Table 2
Synthesis of the main hydrothermal alteration features associated with the Fe-P mineralization types.

Ore type	Na-Ca-Fe Alteration	Fe(±)Ap Stage	K Alteration	Sulfidation Stage
Skarn	Diopside-garnet-actinolite-quartz	Magnetite with poorly developed apatite	Poorly developed	Poorly developed
Massive hematite		Hematite with poorly developed apatite and gorceixite	Poorly developed	Poorly developed
Veins in metadiorite	Diopside-cummingtonite-albite-chlorite	Magnetite with poorly developed apatite	Poorly developed	Poorly developed
Disseminate magnetite in metadiorite	Actinolite-chlorite-albite-epidote	Magnetite with poorly developed apatite	Poorly developed	Poorly developed
Fine grained magnetite-apatite (specular hematite)	Aegirine augite-actinolite-quartz	Magnetite-apatite-(specular hematite)	Poorly developed	Poorly developed
Fe-P stratabound type	Albite-actinolite-chlorite	Magnetite-apatite-monazite	K-feldspar-biotite-magnetite	Bornite-chalcopyrite-chalcocite-covellite-malachite

the stratabound magnetite, mainly those with ilmenite exsolutions, are concentrated in the igneous magnetite field, and the others are between the magmatic-hydrothermal and hydrothermal field. This suggests that there is both hydrothermal and magmatic magnetite in the different mineralizations.

The Al + Mn vs. Ti + V concentrations have been used to compare magnetite from different Fe oxide-apatite occurrence types and magnetite from other mineral systems of hydrothermal and magmatic origins, including skarns, IOCG, Kiruna, and Porphyry Cu deposits (Dupuis and Beaudoin 2011; Nadoll et al., 2014; Dare et al., 2015; Knipping et al., 2015).

In the diagram shown in Fig. 17, vein magnetite is more enriched in Al + Mn and depleted in Ti + V than the magnetite in the host metadiorite, which suggests the different origins or crystallization conditions between them. The magnetite disseminated in the metadiorite is from magmatic crystallization, whereas vein magnetite may have precipitated from high-temperature hydrothermal fluids. The stratabound magnetite type has similar Ti + V values as that of the metavolcanic host rocks (metabasalt-andesitic). It is also richer in these elements than the magnetite megacrystals hosted in the hematite mineralization. In addition, the magnetite megacrystals have practically the same Ti + V values as the host hematite. Finally, the disseminated magnetite of the metadiorite, part of the stratabound mineralization and the metavolcanic host rock of the stratabound mineralization, are concentrated in the Porphyry Cu and Kiruna compositional fields. The magnetite of the veins, skarns, magnetite megacrystals as well as hematite mineralization, are within the metasomatized rock field, and the ilmenite exsolutions, as expected, plots in the field of magmatic rocks.

Knipping et al. (2015), however, use the Cr and V of the magnetite to differentiate the Kiruna type deposits from all other high-temperature deposits, namely, porphyry, IOCG, and Fe-Ti-V/P deposits, owing to the relatively high V (> 500 ppm) and low Cr contents (< 100 ppm) of Kiruna type magnetite (Fig. 18). For these authors, the V content increases with T in magmatic conditions, while it decreases in the IOCG systems. The elevated V concentrations are caused by magnetite crystallization at high temperatures in contrast to magnetite from IOCG deposits that are formed at relatively lower temperatures. The behavior of Cr in magnetite is more controversial. For Dare et al. (2014), the low concentrations of Cr are indicative of hydrothermal magnetite. However, it may be depleted in magnetite from Kiruna-type deposits, either due to fractionation of clinopyroxene or high-temperature hydrothermal process (e.g., Knipping et al., 2015).

In the cases studied, the values of V and Cr are varied. The highest values are related to the exsolutions of ilmenite (V-3148 ppm and Cr-396 ppm) and disseminated magnetite metadiorite (V-2707 ppm and Cr-766 ppm), while the lower ones are in the magnetite skarn, with V (≤ 276 ppm) and Cr (≤ 326 ppm). When plotted in the Cr vs. V diagram of Knipping et al. (2015), only a few samples of the vein and stratabound mineralization are concentrated in the Kiruna ore field. The other samples which have high V (> 500 ppm) and Cr (> 100 ppm) seem to overlap the boundary between high-T hydrothermal and magmatic magnetite formed in Fe–Ti–V and porphyry type, while the samples with V (< 500 ppm) are within IOCG deposit field. In addition, magnetite with low V (< 500 ppm) and Cr content (≤ 326 ppm), a magnetite skarn type, can indicate that magnetite mineralizations with these characteristics are formed by the hydrothermal process. The magnetites that are concentrated in the Kiruna field, with high V and low Cr, respectively, should represent magmatic magnetite overprinted by high-temperature hydrothermal processes (Knipping et al., 2015). Thus, these diagrams show the magnetites of the porphyry, Ti-V-Fe, and Kiruna systems present features that indicate a magmatic origin overprinted by hydrothermal processes. This may highlight that IOA magnetite deposits may have different magmatic affiliations.

Table 3
Chemical composition of representative apatite from the different mineralization types. Element concentrations in wt%. *H2O values by stoichiometry calculation. bd. Below detection.

	Stratabound									
	PR67C2		AM01C3		PR63FC3		PR16C3		AM03C1	
	Rim	Core	Rim	Core	Rim	Core	Rim	Core	Rim	Core
SiO_2	0.007	0.016	0.02	0.071	0.032	0.105	0.028	0.064	0.07	0.064
TiO_2	0.029	0.003	0.075	bd	0.074	bd	0.011	0.035	bd	0.005
Al_2O_3	0.012	0.016	bd	bd	bd	0.014	bd	bd	0.008	bd
FeOt	0.528	0.122	0.072	0.112	0.036	0.099	0.989	0.042	0.871	0.101
MnO	0.059	0.306	0.391	0.517	0.323	0.259	0.066	0.243	0.482	0.325
MgO	0.014	bd	bd	0.022	0.049	0.087	0.022	0.024	0.033	0.004
CaO	54.3	54.42	54.66	53.73	53.56	53.24	53.77	53.7	53.87	54.93
Na_2O	0.058	0.081	0.063	0.079	0.103	0.136	0.099	0.079	0.174	0.161
K_2O	bd	bd	bd	0.006	0.018	0.043	bd	0.005	bd	0.02
P_2O_5	42.1	42.38	42	40.98	39.65	38.38	41.69	43.04	42.01	41.43
Cr_2O_3	bd	bd	0.002	0.006	0.044	bd	0.035	bd	bd	bd
BaO	0.023	0.099	0.002	0	0.066	0.077	0	0	0.08	0
SrO	bd	0	0.07	0.028	0.06	0	0	0.05	0	0.029
V_2O_3	0	0.003	0.047	0.02	0.011	0	0.044	0	0	0.064
NiO	0.062	0.012	0.012	0	0.025	0	0	0	0	0.004
Y_2O_3	0.126	0.126	0.083	0.098	0. 079	0.055	0.04	0.093	0.205	0.166
F	2.90	3	3.7	3.03	3.177	2.993	2.639	2.423	2.756	2.708
Cl	0.22	0.219	0.138	0.154	0.249	0.25	0.237	0.338	0.081	0.123
(OH)	0.947	0.628	0.326	2.5	3.899	5.19	1.529	1.04	0.738	1.189
Total	101.385	101.437	101.671	101.409	101.471	101.372	101.204	101.191	101.384	101.333

Disseminated Vein					Metabasalt-andesitic			Hematite		
	JW12DC4	JW12DC5	JW15C3A Rim	JW15C3B Core	PR63AC2A	PR63AC2B	PR63AC4	CS179C2A Core	CS179C2B Rim	PR01C4
SiO_2	0.011	0.051	0.881	0.865	0.115	0.056	0.178	0.6	0.472	0.114
TiO_2	bd	bd	bd	0.02	0.054	bd	bd	bd	bd	bd
Al_2O_3	bd	bd	bd	0.022	0.014	bd	bd	bd	0.003	0.006
FeOt	0.075	0.09	0.503	0.039	0.263	0.369	0.085	0.51	0.588	0.84
MnO	0.008	0.038	0.078	0.094	0.069	0.142	0.016	0.016	0.082	0.01
MgO	0.023	bd	0.011	0.063	0.003	0.009	bd	bd	0.017	0.039
CaO	54.69	55.09	54.5	54.32	54.52	54.3	54.47	55.1	54.98	53.9
Na_2O	0.049	0.025	0.05	0.057	0.128	0.105	0.03	0.06	0.022	0.037
K_2O	bd	bd	0.005	bd	0.002	bd	0.001	bd	bd	bd
P_2O_5	42.08	41.4	41.66	41.32	39.66	39.93	38.19	41.77	41.52	40.26
Cr_2O_3	bd	bd	0.018	0.016	0.005	0.011	bd	bd	bd	0.065
BaO	bd	bd	bd	bd	bd	0.002	bd	bd	bd	bd
SrO	bd	bd	0.153	0.091	bd	0.019	0.021	0.311	0.201	0.057
V_2O_3	bd	0.013	bd	0.054	0.069	0.055	bd	0.022	0.009	bd
NiO	bd	0.033	0.037	bd	0.036	bd	0.042	bd	0.047	0.102
Y_2O_3	0.017	bd	bd	bd	0.088	0.172	0.16	0.025	0.088	0.037
F	4.12	2.79	0.019	0.033	4.441	3.122	4.689	3.29	3	4.27
Cl	0.043	0.076	2.03	1.98	0.011	0.02933	0.017	0.012	0.036	0.213
(OH)	0.629	1.578	0.576	0.67	2.475	3.161	4.229	0	0	1.92
Total	101.762	101.93	100.537	99.587	101.959	101.496	102.138	101.73	101.07	101.88

Table 4
Chemical composition of representative magnetite and hematite from the different mineralizations types. Element concentrations in wt%. bd. Below detection.

	Mag. xenocrystal		Mag. Skarn		Vein		Metadiorite		Metabasalt-andesitic		
	CS179C3A	CS179C3B	JW13.2C4A	JW13.2C4B	JW15.2C3A Core	JW15.2C3B Rim	JW12.2DC3A	JW12.2DC3B	PR63aC2A	PR63aC3	PR63aC4
SiO_2	bd	0.01	0.016	0.044	0.009	0.017	0.041	0.016	0.043	bd	0.004
TiO_2	bd	bd	0.01	bd	0.003	0.066	bd	0.07	bd	bd	0.133
Al_2O_3	0.059	0.093	0.089	0.006	0.111	0.079	0.043	0.03	0.041	0.031	0.025
FeOt	92.7	92.9	93.4	93.48	90.82	91.66	92.51	93.82	92.81	92.58	92.63
MnO	0.238	0.163	0.053	bd	0.932	0.814	0.421	0.139	0.159	0.046	0.117
MgO	0.02	0.044	0.003	0.024	0.68	0.798	bd	bd	0.04	bd	0.014
CaO	0.012	bd	bd	0.011	bd	bd	0.015	bd	0.011	bd	0.001
Na_2O	bd	0.005	bd	bd	0.024	0.002	0.02	bd	bd	bd	0.055
K_2O	bd	bd	0.044	bd	bd	bd	bd	bd	bd	0.015	bd
P_2O_5	0.032	0.016	bd	bd	bd	0.029	0.016	0.008	bd	0.069	bd
Cr_2O_3	bd	0.046	bd	0.04	0.039	bd	0.061	0.108	0.012	0.019	bd
BaO	0.029	0.131	0.046	bd	0.145	0.047	0.038	bd	bd	bd	bd
SrO	bd	0.13	bd	bd	bd	bd	0.109	bd	0.161	0.003	0.088
V_2O_3	0.055	bd	0.021	0.019	0.134	0.154	0.343	0.387	0.188	0.142	0.194
NiO	bd	bd	0.01	bd	bd	0.006	bd	bd	bd	bd	0.012
F	0.193	0.325	0.23	0.307	0.164	0.324	0.318	0.283	0.239	0.379	0.329
Cl	bd	bd	0.018	bd	0.016	0.011	0.016	bd	bd	bd	bd
ThO_2	bd	bd	bd	bd	0.008	bd	0.005	bd	bd	bd	bd
UO_2	bd	bd	bd	bd	bd	bd	bd	bd	bd	bd	bd
Y_2O_3	bd	0.015	0.043	bd	0.01	bd	0.009	bd	0.004	bd	0.018
Total	93.4	93.9	94.03	93.95	93.23	94.16	94.31	95.25	93.9	93.43	93.8

Stratabound									Rhombohedral hematite			Ilmenite exsolutions		
	AM03C1 Core	AM03C1 Rim	PR67IC2A	PR67IC2B	AM01C3A Rim	AM01C3B Core	PR63FC3A Core	PR63FC3B Rim	PR16C1	PR01C2A Core	PR01C2B Rim	PR01C4	AM03C1	PR67HC3A	PR67HC3B
SiO_2	0.028	0.101	0.02	0.071	0.022	0.036	0.006	0.022	0.031	bd	bd	bd	0.02	bd	0.003
TiO_2	0.111	0.039	0.043	bd	0.078	1.13	bd	bd	0.018	0.011	bd	0.01	45.949	14.2	14.211
Al_2O_3	0.286	0.085	0.037	0.037	bd	7.39	0.023	0.001	0.078	0.175	0.245	0.163	0.059	0.032	0.032
FeOt	92.75	93.02	94.67	94.77	92.39	84.07	94.18	94.88	93.57	90.42	90.41	90.18	35.55	78.28	78.69
MnO	0.017	0.062	0.158	0.175	0.438	0.519	0.639	0.484	0.285	bd	bd	0.056	17.808	0.677	0.768
MgO	0.013	bd	0.017	0.026	0.01	0.082	0.04	0.091	bd	0.023	0.016	0.001	0.022	0.041	0.001
CaO	bd	bd	bd	bd	bd	bd	bd	0.046	bd	bd	0.001	0.002	0.081	0.038	bd
Na_2O	bd	bd	0.021	bd	0.016	0.057	0.019	0.024	0.017	bd	0.018	bd	0.021	0.04	bd
K_2O	bd	bd	bd	0.005	0.039	bd	bd	0.004	bd	bd	0.029	bd	bd	bd	bd
P_2O_5	0.03	0.041	0.043	bd	bd	0.009	bd	0.058	0.019	0.059	0.013	0.042	bd	0.029	0.04
Cr_2O_3	0.036	0.038	0.011	0.031	0.012	bd	0.019	0.029	bd	bd	bd	bd	0.024	0.037	0.006
BaO	0.033	0.102	bd	0.047	0.023	0.06	bd	0.007	bd	bd	bd	0.092	0.264	bd	0.045
SrO	bd	0.018	bd	bd	bd	bd	bd	bd	0.015	bd	0.017	bd	bd	0.066	bd
V_2O_3	0.142	0.131	0.047	0.013	0.079	0.069	0.14	0.048	0.096	0.034	0.048	bd	0.25	0.261	0.318
NiO	bd	bd	0.066	bd	0.044	bd	0.081	0.028	0.004	bd	bd	0.02	bd	bd	0.056
F	0.247	0.268	0.289	0.272	0.283	0.204	0.357	0.309	0.311	0.262	0.318	0.276	bd	0.159	0.307
Cl	bd	bd	bd	bd	0.041	0.012	bd	0.005	bd	bd	bd	0.016	0.02	bd	bd
ThO_2	0.006	bd	bd	0.024	0.012	0.001	bd	bd	bd	bd	0.008	bd	bd	bd	bd
UO_2	bd	bd	bd	bd	bd	bd	bd	bd	bd	bd	bd	bd	bd	bd	bd
Y_2O_3	0.014	0.008	0.017	0.016	0.043	bd	0.029	0.042	bd	bd	bd	bd	bd	bd	bd
Total	93.85	94.05	95.49	100.16	95.55	93.72	95.67	96.13	94.54	91.02	91.17	90.86	100.32	94.12	94.79

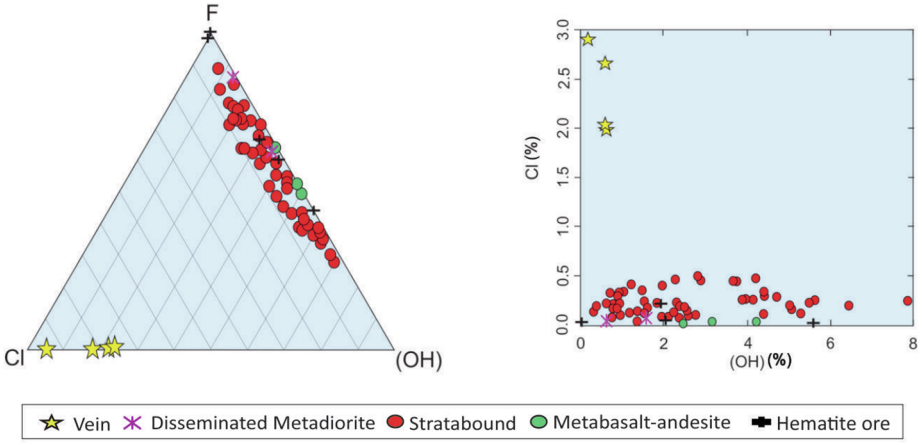

Fig. 13. Compositional range of apatite of different Fe-P mineralization types in terms of F-Cl-OH (%) (A) and Cl vs. OH (B).

7.4. Zircon U-Pb geochronology

Zircon crystals of the metarhyolite sample (R-27), the stratabound mineralization host rock, are dominantly colorless with sizes between 100 and 200 µm. CL images show subhedral to euhedral shape, sometimes well elongated, with xenocrystic nuclei, often with oscillatory zoning or with irregular domains suggesting rapid crystallization (e.g. Corfu et al., 2003). The population of zircon crystals display a Th/U ratios range from 0.19 to 0.74 (Supplementary Table 7) and a concordant age of 554 ± 6 Ma (MSWD = 1.7), interpreted as crystallization age (Fig. 19a).

Zircons from biotite granite (R-28) that crosscuts the stratabound mineralization present a more heterogeneous population, with colorless to pale yellow grains, size around 300 µm. CL images show some zircons with more rounded edges, varying length/width ratios and others with bi-terminations, sometimes zoned and with some fractures. The zircon crystals present Th/U ratios between 0.02–0.24 and a concordant age of 548 ± 3 Ma (MSWD = 8.7) indicating a post-Braziliano age (Fig. 19b).

8. Discussion and implications for ore genesis of the Fe-P-(Cu) mineralizations

The mineralization styles combined with petrographic, mineralogical and mineral chemistry data suggest that the five Fe-P-(Cu) occurrences defined in the SQMA are the product of several different mineralizations forming episodes.

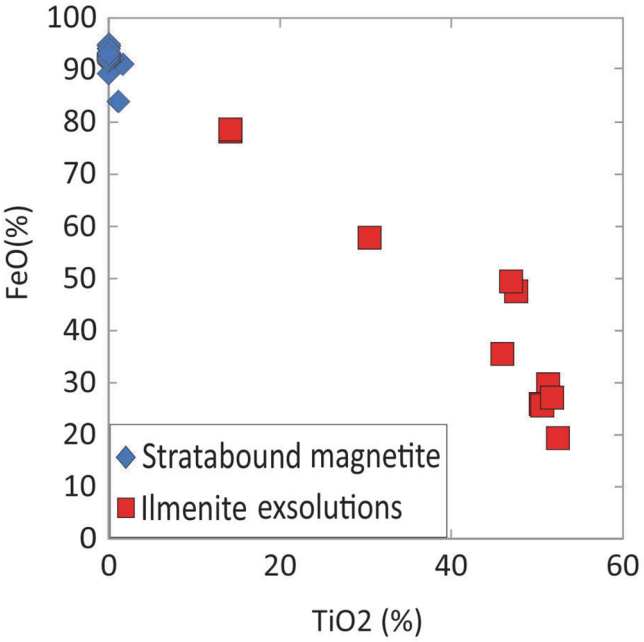

Fig. 15. Concentrations of FeO vs TiO_2 in magnetite and ilmenite exsolutions from the stratabound Fe-P mineralization.

8.1. Stratabound mineralization

The stratabound mineralization Fe- and P-rich corresponds to one of the older occurrences. It is hosted in a sequence bimodal mafic-felsic

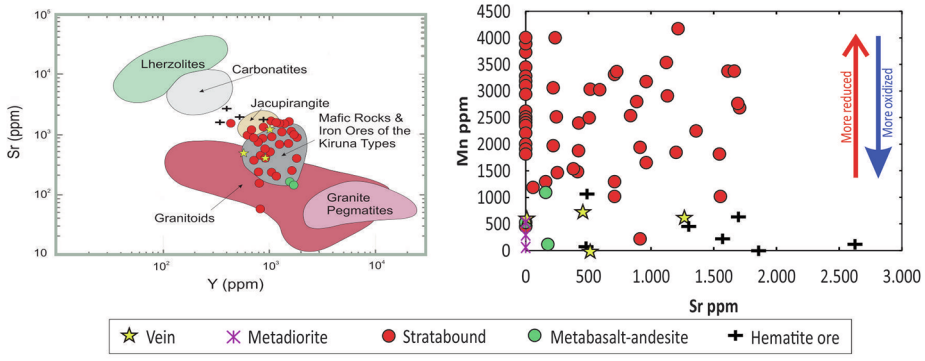

Fig. 14. Sr vs. Y (A) and Mn vs. Sr (B) discrimination diagrams for apatite from the different Fe-P mineralization types, compared to intrusive rocks and Kiruna-type Fe ore from Belousova et al. (2002).

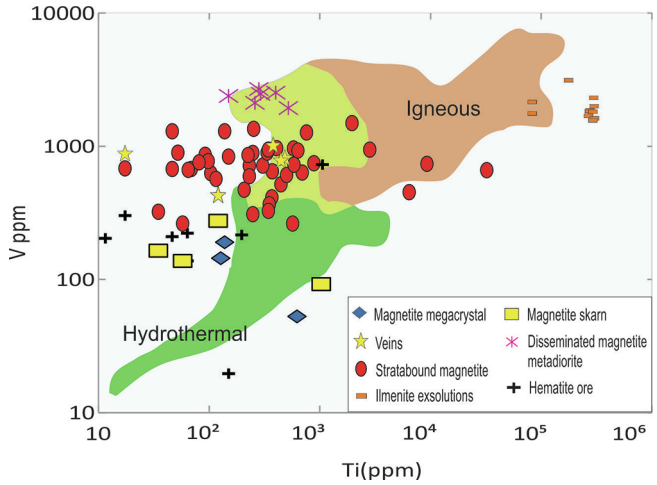

Fig. 16. V vs. Ti ppm concentrations in magnetite from the different Fe-P mineralization types investigated in the western sector of the SQMA (adapted from Nadoll et al., 2015).

subvolcanic rocks deformed and partially modified by metamorphism and hydrothermalism. The oxide-apatite ore is also deformed and registers the same deformation style that host rocks that suggests a close relationship with this bimodal magmatism (Fig. 4B, E and F). Magnetite globules within felsic rocks also indicate contemporaneity between both. Most magnetite presents magnetite-ilmenite intergrowth trellis and sandwich texture. Namesake textures have been used as a Fe-Ti oxide geothermometer and indicate equilibrium temperatures above 600 °C (Lepage, 2003; Tan et al., 2016) that suggest a feature of magmatic magnetite or magnetite formed in metamorphic conditions of high amphibolite to granulite facies (e.g Harlov, 2000). Considering that the peak of the metamorphism happened around 600 Ma and the age of its host rock is younger (~550 Ma) it is probable that this mineralization is of magmatic origin. By the way, a genetic link of this occurrence with the metadioritic mineralization is suggested since its composition, the crystallization sequence between magnetite and silicate phases wherein magnetite incorporates the early plagioclase and clinopyroxene, and the composition of the apatite in both mineralizations are similar (Fig. 13A, and B). So the metabasalt-andesitic intermediate to mafic host rocks could be considered the volcanic equivalents of the metadiorite. Thus, the Fe-P stratabound mineralization shows a preference for the most basic-intermediate volcanic rocks which can be treated as a product of basic tholeiitic magma differentiation under reduced, dry and low oxygen fugacity conditions, whose residual liquids are rich in FeO (ferrous iron) and poor in silica (Grant, 1984). The presence of manganese-rich apatite suggests its crystallization from a reduced environment or source. However, tholeiitic magma is poor in P, so that the phosphorus in that rock can be the result of crustal contamination. The presence of apatite marbles in the nearby Ceará Complex could reinforce these arguments (Veríssimo et al., 2016).

Padilha et al. (2017) interpreted important magnetotelluric anomalies in the AMSQ region, where these occurrences are located, as lithospheric megastructures. These structures could be favorable to the channeling of magmatic associations and of magmatic and non-magmatic fluids that when assimilating P of their hosts rocks could form these important mineral occurrences.

In addition, the textural variation found in this stratabound mineralization, such as fine granulation at the contact zones, and thicker granulation in farther zones, has been found in other IOA deposits, and has been interpreted as magmatic in origin, with the fine-grained zone representing a chilled margin, and the coarse-grained zone the central part of a magma cooling (e.g., Nold et al., 2013). This suggests a history of differentiated cooling during the emplacement of the mineralized body, characteristic of magmatic mineralization. On the other hand, the presence of monazite along the microfractures and grain boundaries in these apatites indicates that they were rich in REE, which was metasomatically removed from apatite to form other REE-bearing minerals, such as monazite (e.g., Harlov et al., 2002). Thus, the chemical data of apatite and magnetite of the stratabound ore indicate a magmatic origin, but it is partially modified by the hydrothermal processes. This allows the comparison to the stratiform or stratabound deposits of Kiruna (Sweden) and Bafq (Iran), Pea Ridge and Pilot Knob IOA deposits in Missouri, United States.

On the other hand, copper sulfide mineralization is localized and seems to be genetically related to the influence of the biotite granite that crosscuts the stratabound ore, indicating a late process in relation

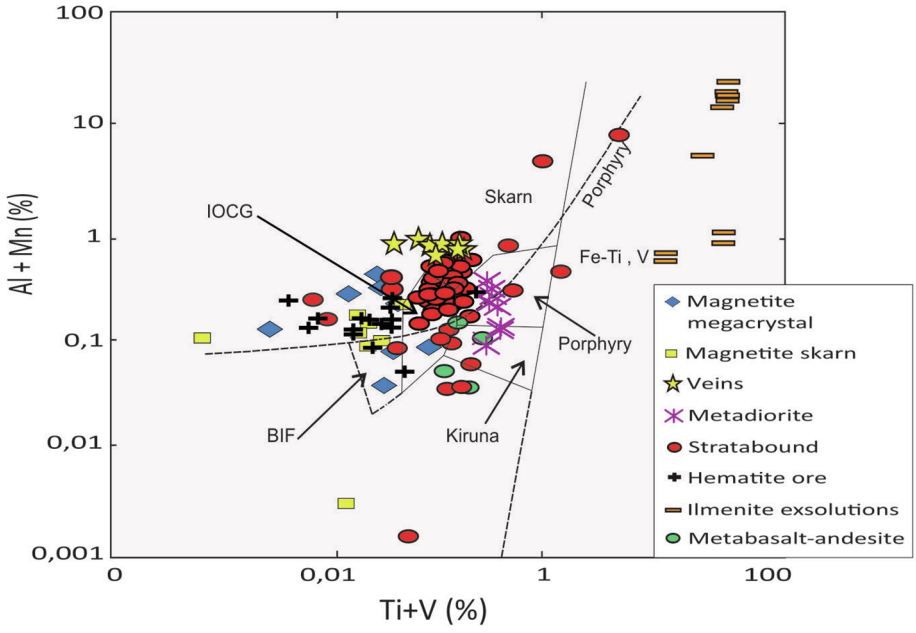

Fig. 17. Al + Mn% vs. Ti + V% discrimination diagram for the studied iron oxide mineralizations of Ararendá compared to the oxides from Kiruna, IOCG systems, porphyry copper deposits, skarns, and BIF (Adapted from Dupuis and Beaudoin, 011, and Nadoll et al., 2014).

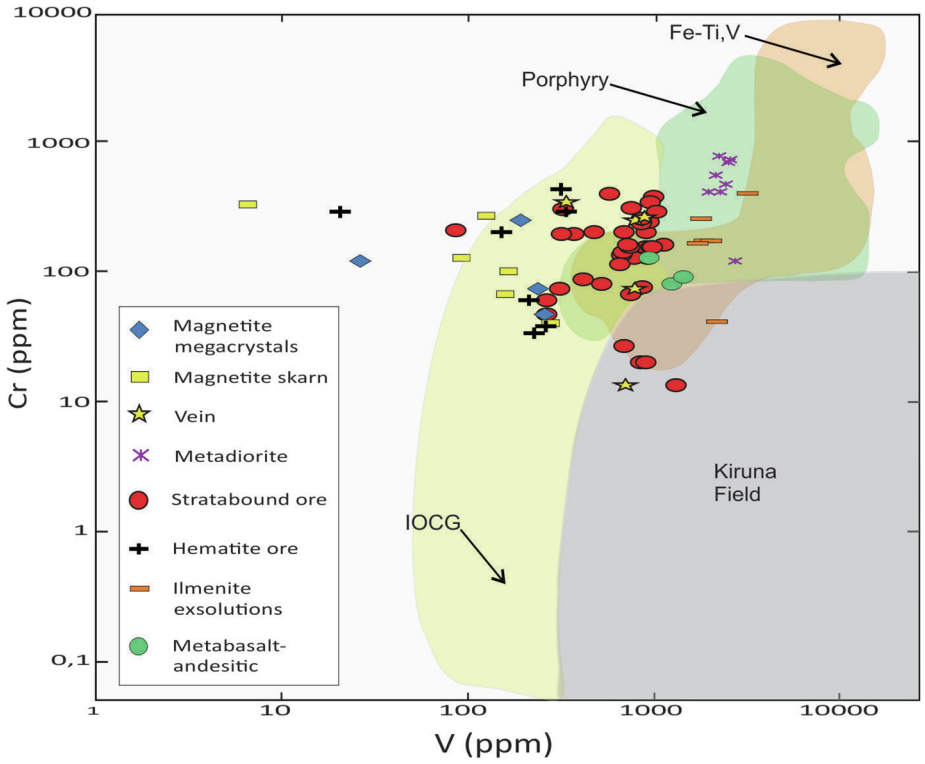

Fig. 18. Cr vs. V ppm concentrations in magnetite from the different Fe-P mineralization types investigated in the western sector of the SQMA (Adapted from Knipping et al., 2015).

to that stratabound type. The geochronological age obtained in the metarhyolites (554 ± 6 Ma), which, by formation, are synchronous to the host metabasalt-andesitic of the stratabound mineralization, and the biotite granite (548 ± 4 Ma) that crosscuts this mineralization, confirm this relation.

8.2. Fine-grained massive magnetite-(specular hematite)-apatite

The fine-grained massive magnetite-apatite mineralization that is slightly deformed, with primary features, such as volatile escape vesicles, and fibro-radial aggregates of aegirine at the matrix, suggests an enrichment of fluids in Na, Fe, Si, halogens, and H_2O, compatible with a similar volcanic activity that occurred at the El Laco deposit, in Chile. The type with specular hematite, epidote/actinolite, and apatite in various habits, subhedral to anhedral with amorphous apatite rings around crystals of limonitized iron oxides, defines a zone of P and Fe-rich hydrothermal fluids. Therefore, the fine-grained magnetite-apatite and magnetite-hematite-apatite types appear to develop at epizonal levels and form part of the same magnetitic-phosphate system that gave rise to the stratabound mineralization. In this case, one can treat it as a product of the evolution of a continuum of the Fe-P system, in which it would represent the extrusive phase, channeled along major faults, while stratabound ore would be the deepest or subvolcanic phase.

8.3. Disseminated and vein magnetite in albitized metadiorite

The disseminated and vein-type occurrences in metadiorite rocks seem to show the same magmatic affiliation but in different crystallization conditions. The first origin is igneous and the second is magmatic-hydrothermal. The occurrence of the vein type can represent late-magmatic injections or is a product of crystallization of high-temperature saline hydrothermal-magmatic fluids (e.g., Zhao et al. 2017). The presence of the Cl-rich apatites restricted to these veins reveals the feature of hydrothermal-magmatic fluids or even saline fluids involved in their formation indicating these are hydrothermal (e.g., Xavier et al., 2011, Edfelt, 2007). However, the low-temperature assemblage, composed of chlorite, albite, and epidote that overprints the high-temperature assemblage, can be the result of the interaction with meteoric fluids and/or host rocks developed, under shallow crust conditions and lower temperature, which induced a pervasive alteration in the metadiorite. Therefore, the association of this mineralization with dioritic rocks and the style of the ore in disseminated and vein form allows us to compare this occurrence to the Gushan magnetite-apatite deposit in China (e.g., Hou et al., 2011).

8.4. Massive hematite

The massive hematite mineralization, dominated by rhombohedral hematite with polygonal texture, is more debatable. The polygonal texture, which is indicative of textural equilibrium and generally reflects the recrystallization of minerals, has been treated in the literature as metamorphic, metasomatic and magmatic (Nold et al., 2013). The magmatic texture is formed when textural equilibrium still occurs in the final stage of magmatic consolidation (e.g., Best, 2003). In the metamorphic hypothesis, the polygonal texture has been interpreted as: i) associated with crystallization/recrystallization under static conditions, related to thermal metamorphism (low P and high T); and ii) related to the annealing process, associated with recrystallization, implying a reduction in the surface of irregular grains accompanied by the elimination of the smaller grains (Passchier and Trouw, 2005). In the case of iron ores with these texture aspects, two models have been proposed for their formation: a) annealing at high T in a closed system; and b) substitution involving fluids in an open system or hydrothermal process (e.g., Ciobanu and Cook, 2004).

The hematite mineralization often contains relict magnetite grains that are deformed and martitized, suggesting that magnetite was replaced by hematite in the oxidation reaction, a pseudomorphic replacement, where the oxidation reaction follows the (1 1 1) planes of primary magnetite (e.g., Mücke and Cabral, 2005). The subsequent metamorphism should cause the recrystallization of martite-textured

hematite into coarse-grained hematite (annealing model in high T). However, the chemical composition difference between the relict magnetite crystals and the twinned hematite suggest the substitution involving fluids in a hydrothermal system (e.g., Ciobanu and Cook, 2004; Hu et al., 2014). In this case, it may be thought that hydrothermal fluids, due to the influence of T, salinity, and oxygen fugacity, may promote the dissolution of primary magnetite (e.g., Hemley and Hunt, 1992). An increase in T could increase solubility, promoting the

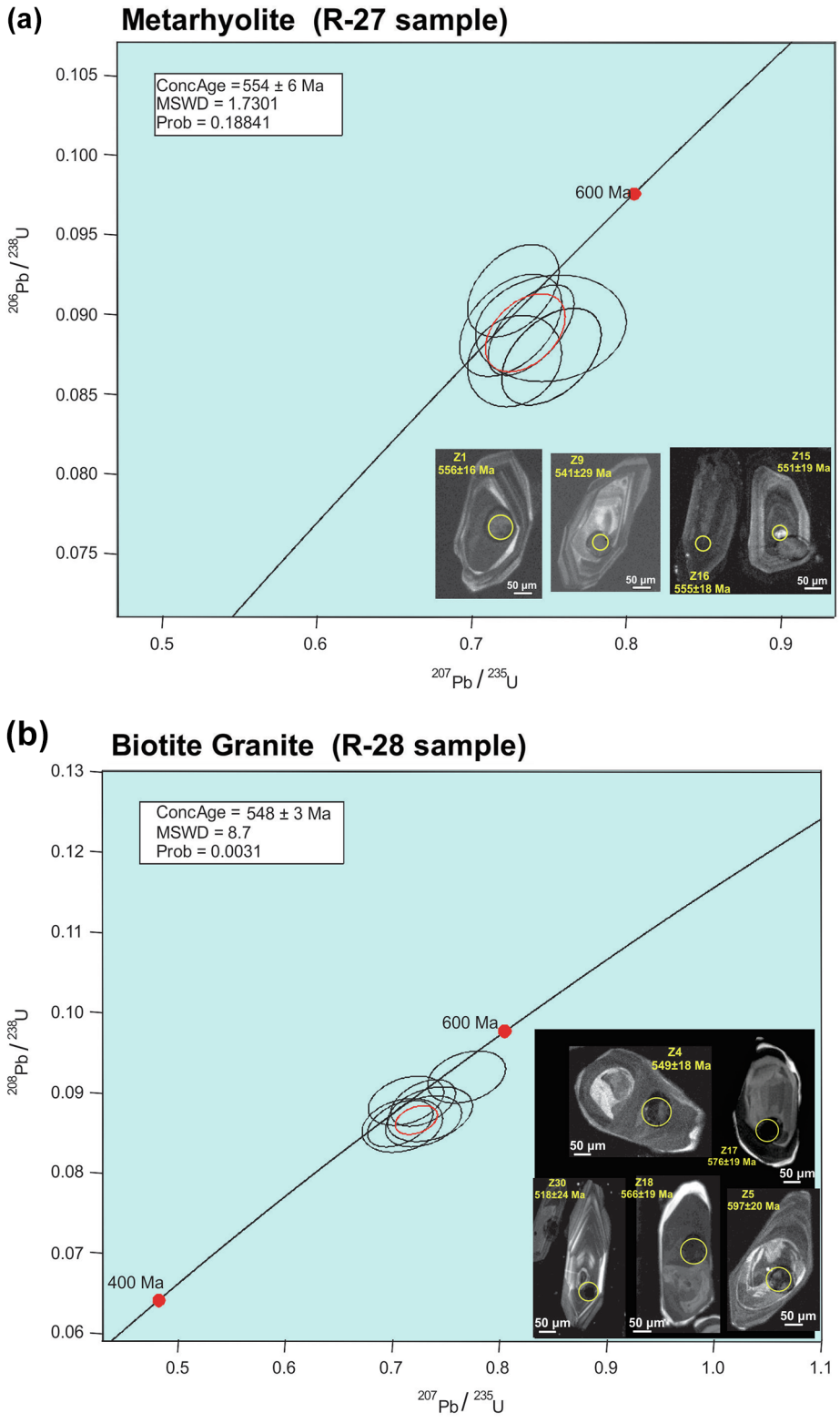

Fig. 19. LA-ICP-MS U–Pb analyses and textural features of zircon of metarhyolite and biotite granite samples. (A) U-Pb Concordia diagram for metarhyolite (sample R-27) with a crystallization age of 554 ± 6 Ma (MSWD = 1.7). At the lower corner, cathodoluminescense image (CL) of zircon of metarhyolite; (B) Concordia diagram for biotite granite (sample R-28) with a crystallization age of 548 ± 3 Ma (MSWD = 8.7). At the lower corner, cathodoluminescense image (CL) of zircon of biotite granite.

dissolution of primary magnetite and the formation of secondary varieties. The biotite granite that cuts the stratabound mineralization could be the inducing agent of this process. The superposition of high T saline fluids derived from the cooling granitic magma could cause the iron oxide to dissolve and then reprecitate in more oxidant conditions (e.g., Hu et al., 2014). Therefore, by the present level of knowledge, it can be assumed that the studied hematitic mineralization is associated with T-high hydrothermal fluids. The presence of quartz veins in association with massive hematite supports this hydrothermal origin (Fig. 9B).

On the other hand, except for the iron deposits of Pilot Knob and Iron Mountain in Southeastern Missouri (USA) (e.g., Nold et al., 2014), and Grängesberg in Sweden, the examples of deposits bearing rhombohedral hematite seem to be rare, which makes this occurrence an exceptional case.

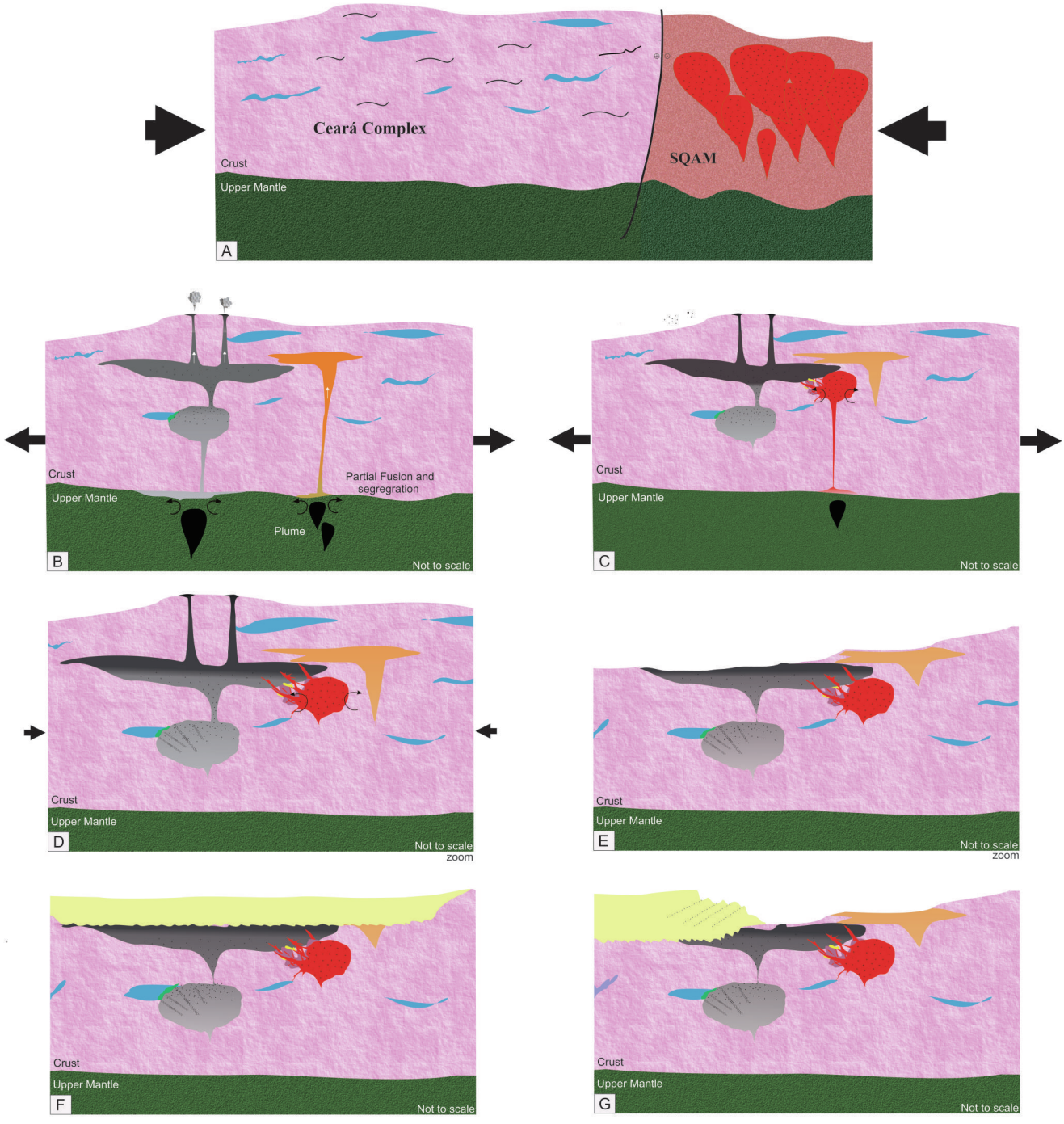

(caption on next page)

Fig. 20. Proposed model for the evolution of the different IOA mineralization types in the Santa Quitéria magmatic arc. A Pre-mineralization geological setting: Ceará Complex and Santa Quitéria magmatic arc in tectonic contact on the Brazilian event (~600 Ma). B Rise in Fe-rich mafic magma with crustal phosphorous contamination that gave origin to diorite and basalt-andesite volcanic rocks in a post-collisonal tectonic regime within the Ceará Complex. C Fractional crystallization with early crystallization of anhydrous minerals (clinopyroxene and plagioclase) and the onset of disseminated magnetite precipitation during ferrodioritic magma emplacement. This is followed by subsequent segregation of volatile-rich iron-oxide residual melt, a chemically immiscible process, triggered by addition of phosphorus by crustal contamination, which favors precipitation of massive stratabound magnetite-apatite mineralization at shallower crustal levels. As this happens more residual volatile-rich fluid (containing Fe, P, Si, Na, halogens, H_2O) are accumulating, which by decompression causes the focusing of residual volatile-rich fluid along small faults and fractures. It produces a fine-magnetite and apatite mineralization with aegirine in fiber-radial aggregates, actinolite, hematite, epidote, and quartz in vesicles or amygdala. Onset of Post-Brasiliano granitic magmatism. D. Post-Brasiliano Granite intrusion that crosscut the stratabound mineralization. Development of a thermo-metamorphic aureole in the contact between granite and stratabound mineralization marked by magnetite and apatite recrystallization, accompanied by localized potassic alteration and sulfidation. In more distal zones the influence of this intrusion was likely responsible for the development of rhombohedral hematite with polygonal texture with relict magnetite. E and F. Erosion and thermal subsidence followed by the deposition of the sedimentary sequence of the Silurian Parnaíba Basin, which extends over the mineralized zones. G. Uplift and erosion of the Parnaíba Basin with exposure of the IOA-type mineralization.

8.5. Magnetite-garnet

The massive magnetite-garnet occurrence is of the skarn type that, given its proximity to the metadiorite, may be interpreted as the exoskarn. The presence of high-T Ca-Na-Fe and low-T mineral aggregates characteristic of progressive and retrograde reactions, respectively, common in deposits of skarns formed by contact metamorphism (e.g., Meinert et al., 2005), support these arguments.

Collectively, these data allow us to propose the following multistage evolution model for the different IOA type mineralization of the Santa Quitéria magmatic arc:

1. After the apex of the Brasiliano orogeny (ca. 600 Ma), the change from frontal to oblique collision at ca. 580 Ma within the Borborema Province triggered the formation of large continental-scale shear zones and several late-tectonic granites aged between 580 and 560 Ma, which went followed by post-collisional to anorogenic granites (< 550 Ma) (dos Santos et al., 2008; Arthaud et al., 2015) (Fig. 20A).
2. The evolution of the Estreito Unit initiates with the formation of extensional structures associated with the development of these later shear zones. Mantle underplating would cause partial melting of the crust, segregation, and rise of bimodal magmatism along of these structures (Fig. 20B). It follows the contamination of iron-rich mafic or intermediate magma with crustal phosphorus within the Ceará Complex.
3. The early crystallization of the ferrodioritic or intermediate magma during your emplacement initiates with anhydrous minerals (clinopyroxene and plagioclase) and some disseminated magnetite. This is followed by segregation of a volatile-rich residual iron oxide melt, a chemically immiscible process, triggered by the addition of phosphorus by crustal contamination and the precipitation of massive magnetite (Fe-P stratabound mineralization) at shallower crustal levels (Fig. 20C). After the continuous accumulation of more volatile-rich fluid containing Fe, P, Si, Na, halogens, and H_2O follows later decompression that induces the migration of residual volatile-rich fluid along small fractions and fractures. The result is fine-magnetite and apatite mineralization with aegirine in fiber-radial aggregates, actinolite, hematite, epidote, and quartz in vesicles or amygdala, representative these magmatic-hydrothermal or hydrothermal process.
4. The onset of late felsic magmatism represented by granite intrusions may have promoted the development of a thermo-metamorphic aureole along intrusion contacts marked by magnetite and apatite recrystallization, accompanied by localized potassic alteration and sulfidation (Fig. 20C, 20D). In more distal zones the influence of this intrusion would be likely responsible for the development of rhombohedral hematite with polygonal texture with relict magnetite.
5. The final stage is marked by erosion and thermal subsidence followed by the deposition of the first sedimentary sequences of the Silurian Parnaíba Basin, which extends over the mineralized zones (Fig. 20E, F). This may have contributed to the preservation of sulfide mineralization from oxidation and weathering after its formation near the surface. Subsequently, the sedimentary cover would be eroded, triggering the exposure of the mineralization (Fig. 20G). Fig. 20 summarizes, in an integrated scheme, the proposal of evolution for these different types of mineralizations.

9. Conclusions

The geological, petrographic, and mineral chemical data indicate that the five Fe-P-(Cu) mineralizations defined on the western boundary of the SQMA are the product of several different ore-forming episodes. They form at different crustal levels, ranging from intermediate to shallow crustal levels in association with bimodal subvolcanic sequences and dioritic intrusions, with ages of approximately 554 ± 6 Ma. The Fe-P-(Cu) mineralization occurs as massive bodies, veins or disseminated, associated with Na and Na-Ca-Fe pervasive alteration and a localized K-alteration. In addition, the textural aspect and compositional data of apatites and magnetites in the ore indicate that the stratabound and metadiorite-disseminated magnetite mineralization exhibits magmatic affiliation, overprinted by fluids of magmatic-hydrothermal origin and probably developed at deep crustal levels. The fine-grained massive magnetite-apatite type, with and without specular hematite, and some cavities that seem to be vesicles formed by the escape of volatiles reflect a volatile-rich iron-oxide melt developed at epizonal levels but that should be part of the same magnetite-apatite system that gave rise to the stratabound ore. The copper sulfide mineralization is localized and seems to be genetically related to the late- to post-Brazilian biotite granite of age 548 ± 3 Ma that crosscuts the stratabound ore, indicating a late process in relation to that stratabound mineralization. The vein-type magnetite mineralization in metadiorite rocks is hydrothermal in origin. The massive hematite ore dominated by rhombohedral hematite with polygonal texture with relict magnetite grains is associated with high-T hydrothermal processes. The skarn occurrences are products of metasomatic interaction between metadiorite rocks and calc-silicate rocks.

The mineral chemistry data also shows that magnetite of magmatic origin in the deposits of the IOA type can have different chemical composition, whose difference may be associated with its magmatic affiliation. Some are of tholeiitic and/or calcium-alkaline filiation and others of alkaline affiliation.

In the tectonic context the shear zones played an important role in the channeling of magmatism and hydrothermal fluids. The Iron and apatite mineralizations are associated with the discontinuity of the earth's crust that marks the tectonic boundary between the Parnaiba Block, located in the west and the Ceará Central Block, to the east.

The recognition of IOA occurrences in the Santa Quitéria magmatic arc is of great importance because it provides a prospective guide for the characterization of these deposit types in the Santa Quitéria magmatic arc in Borborema Province. It opens the possibility for the

exploration of IOCG-type deposits in this tectonic domain amplifying the geological and metallogenetic knowledge about these deposits and corresponds to the first description of the IOA deposits in Brazil.

Acknowledgments

The authors thank CNPq (Proc. 481713/2013-1), the National Institute of Science and Technology of Tectonic Studies (CNPq/INCT-ET/Proc.573713/2008-1), PROCAD/NF (UFC-UnB), CAPES, Federal University of Ceará, University of Brasília and the University of Campinas for support technical and laboratory. We also acknowledge to Gabriel Valentim and the reviewers of the Ore Geology Reviews for their constructive comments that greatly enriched the work.

Appendix A. Supplementary data

Supplementary data to this article can be found online at https://doi.org/10.1016/j.oregeorev.2019.103024.

References

Amaral, W.S., 2010. Análise Geoquímica, Geocronológica e Termobarométrica das Rochas de alto Grau Metamórfico, Adjacentes ao Arco Magmático de Santa Quitéria, NW da Província Borborema. PhD Thesis. Instituto de Geociências, Universidade Estadual de Campinas, Brasil.

Archanjo, C.J., Launeau, P., Hollanda, M.H.B.M., Macedo, J.W.P., 2009. Scattering of magnetic fabrics in the Cambrian alkaline granite of Meruoca (Ceara State, northeastern Brazil). Int. J. Earth Sci. 98, 1793–1807.

Arthaud, M.H., 2007. Evolução Neoproterozóica do Grupo Ceará (Domínio Ceará Central, NE Brasil): da Sedimentação à Colisão Continental Brasiliana. PhD thesis. Universidade de Brasília, Brasília, pp. 170.

Arthaud, M.H., Caby, R., Fuck, R.A., Dantas, E.L., Parente, C.V., 2008. Geology of the Northern Borborema Province, NE Brazil and its correlation with Nigeria, NW AfricaWest Gondwana: Pre-Cenozoic Correlations Across the South Atlantic Region, 1a ed. Geological Society of London, Londres, pp. 49–67 vol. 294.

Arthaud, M.H., Fuck, R.A., Dantas, E.L., Santos, T.J.S., Caby, R., Armstrong, R., 2015. The Neoproterozoic Ceará Group, Ceará Central domain, NE Brazil: depositional age and provenance of detrital material. New insights from U-Pb and Sm-Nd geochronology. J. South Am. Earth Sci. 58, 223–237.

Barton, M.D., Johnson, D.A., 1996. Evaporitic source model for igneous related Fe oxide–(REE–Cu–Au–U) mineralization. Geology 24, 259–262.

Barton, M.D., Johnson, D.A., 2000. Alternative brine sources for Fe oxide (Cu-Au) systems: Implications for hydrothermal alteration and metals. In: In: Porter, T.M. (Ed.), Hydrothermal iron oxide copper-gold and related deposits: A global perspective, vol. 1. Australian Mineral Foundation, Adelaide, pp. 43–60.

Barton, M.D., 2014. Iron oxide (Cu–Au–REE–P–Ag–U–Co) systems. Treatise in Geochemistry Volume 13, 515–541.

Belousova, E.A., Griffin, W.L., O'Reilly, S.Y., Fisher, N.I., 2002. Apatite as an indicator mineral for mineral exploration: trace-element compositions and their relationship to host rock type. J. Geochem. Explor. 76 (2002), 45–69.

Best, M.G., 2003. Igneous and Metamorphic Petrology, 2ª ed. Blackwell Publishing, pp. 729.

Castro, N.A., 2004. Evolução Geológica Proterozóica da Região entre Madalena e Taperuaba, Domínio Tectônico Ceará Central (Província Borborema). Tese de doutorado. Universidade de São Paulo, São Paulo, pp. 221.

Castro, N.A., Ganade de Araujo, C.E., Basei, M.A.S., Osako, L.S., Nutman, A., Liu, D., 2012. Ordovician a-type granitoid magmatism on the Ceara Central Domain, Borborema Province, NE-Brazil. J. South Am. Earth Sci. 36, 18–31.

Cavalcante, J.C., Vasconcelos, A.M., Medeiros, M.F., Paiva, I.P., Gomes, F.E.M., Cavalcante, S.N., Cavalcante, J.E., Melo, A.C.R., Duarte Neto, V.C., Benevides, H.C., 2003. Mapa Geológico do Estado do Ceará – Escala 1: 500.000. Fortaleza, Ministério das Minas e Energia/Companhia de Pesquisa de Recursos Minerais.

Chen, H., 2013. External sulphur in IOCG mineralization: Implications on definition and classification of the IOCG clan. Ore Geol. Rev. 51, 74–78.

Ciobanu, L.C., Cook, N.J., 2004. Skarn Textures and a Case Study: the Ocna de Fier-Dognecea Orefield, Banat, Romania. Ore Geol. Rev. 24, 315–370.

Corriveau, L., 2007. Iron Oxide-copper-gold (± Ag ± Nb ± P ± REE ± U) Deposits: A Canadian Perspective. In: Goodfellow, W.D. (Ed.), Mineral Deposits of Canada: A Synthesis of Major Deposit-types, District Metallogeny, The Evolution of Geological Provinces and Exploration Methods. Geological Association Canada, Mineral Deposit Division, pp. 307–328 Special Publication 5.

Corfu, F., Hanchar, J.M., Hoskin, P.W.O., Kinny, P., 2003. Atlas of zircons textures. In: In: Hanchar, J.M., Hoskin, P.W.O. (Eds.), Zircon. Reviews in Mineralogy and Geochemistry 53. Mineralogical Society of America, and the Geochemical Society, Washington, D.C., pp. 469–500.

Corriveau, L., Montreuil, J.F., Potter, E.G., 2016. Alteration facies linkages among iron oxide copper-gold, iron oxide-apatite, and affiliated deposits in the great bear magmatic zone, Northwest Territories, Canada. Econ. Geol. 111, 2045–2072.

Costa, F.G., Ganade de Araújo, C.E., Amaral, W.D.S., Vasconcelos, A.M., Rodrigues, J.B., 2013. Idade U-Pb (LA-ICPMS) em zircão e isótopos de Nd para granitoides do Complexo Tamboril-Santa Quitéria, Domínio Ceará Central: implicações para magmatismo neoproterozoico sin-colisional no domínio norte da Província Borborema. Geologia. USP Série Científica 13, 159–174.

Dare, S.A.S., Barnes, S.-J., Beaudoin, G., Méric, J., Boutroy, E., Potvin-Doucet, C., 2014. Trace elements in magnetite as petrogenetic indicators. Miner. Deposita 49 (7), 785–796.

Dare, S.A.S., Barnes, S.-J., Beaudoin, G., 2015. Did the massive magnetite "lava flows" of El Laco (Chile) form by magmatic or hydrothermal processes? new constraints from magnetite composition by LA-ICP-MS. Miner. Deposita 50, 607–617.

Dupuis, C., Beaudoin, G., 2011. Discriminant diagrams for iron oxide trace element fingerprinting of mineral deposit types. Miner. Deposita 46, 319–335.

Edfelt, A., 2007. The Tjårrojåkka Apatite-Iron and Cu (-Au) Deposits, Northern Sweden. Thesis for the Degree of Doctor of Philosophy. Division of Ore Geology and Applied Geophysics Luleå University of Technology, pp. 167.

Fetter, A.H., 1999. U-Pb and Sm-Nd Geochronological Constraints on the Crustal Framework and Geologic History of Ceara State, NW Borborema Province, NE Brazil: implications for the Assembly of Gondwana. PhD. thesis. Dept of Geology, Kansas University, USA, pp. 164.

Fetter, A.H., Santos, T.J.S., Van Schmus, W.R., Hackspacher, P.C., Brito, Neves B.B., Arthaud, M.H., Nogueira, Neto J.A., Wernick, E., 2003. Evidence for Neoproterozoic continental arc magmatism in the Santa Quitéria Batholith of Ceará State, NW Borborema Province, NE Brazil: implications for the assembly of West Gondwana. Gondwana Res. 6 (2), 265–273.

Frietsch, R., Perdahl, J.-A., 1994. Rare earth elements in apatite and magnetite in Kiruna-type iron ores and some other iron ore types. Ore Geol. Rev. 9, 489–510.

Ganade de Araujo, C.E., Cordani, U.G., Weinberg, R.F., Basei, M.A., Armstrong, R., Sato, K., 2014. Tracing Neoproterozoic subduction in the Borborema Province (NE-Brazil): clues from U-Pb geochronology and Sr-Nd-Hf-O isotopes on granitoids and migmatites. Lithos 202–203 (2014), 167–189.

Garcia, M.G.M., Arthaud, M.H., 2004. Caracterização de trajetórias P-T em nappes brasilianas: região de Boa Viagem/Madalena – Ceará Central (NE Brasil). Revista de Geologia – UFC 17 (2), 173–191.

Grant, F.S., 1984. Aeromagnetics, geology and ore environments, i. Magnetite in igneous, sedimentary and metamorphic rocks: an overview. Geoexploration 23 (1984/85), 303–333.

Groves, D.I.P., Bierlein, F.P., Meinert, L.D., Hitzman, M.W., 2010. Iron oxide copper–gold (IOCG) deposits through Earth history; implications for origin, lithospheric setting, and distinction from other epigenetic iron oxide deposits. Econ. Geol. 105, 641–654.

Harlov, D.E., 2000. Titaniferous magnetite–ilmenite thermometry and titaniferous magnetite–ilmenite–orthopyroxene–quartz oxygen barometry in granulite facies gneisses, Bamble Sector, SE Norway: implications for the role of high-grade CO_2-rich fluids during granulite genesis. Contrib. Mineral. Petrol 139 (2), 180–197. https://doi.org/10.1007/PL00007670.

Harlov, D.E., Andersson, U.B., Förster, H.J., Nyström, J.O., Dulski, P., Broman, C., 2002. Apatite-monazite relations in the Kiirunavaara magnetite-apatite ore, northern Sweden. Chem. Geol. 191, 47–72.

Hawkes, N., Clark, A., Moody, T.C., 2002. Marcona and Pampa de Pongo: giant Mesozoic Fe-(Cu, Au) deposits in the Peruvian Coastal Belt. In: In: Porter, T.M. (Ed.), Hydrothermal Iron Oxide Copper-Gold and Related Deposits: A Global Perspective Vol. 2. PGC Publishing, Adelaide, pp. 115–130.

Hemley, J.J., Hunt, J.P., 1992. Hydrothermal ore-forming processes in the light of studies in RockBuffered Systems: II. Some general geologic applications. Econ. Geol. 87, 23–43.

Hitzman, M.W., Oreskes, N., Einaudi, M.T., 1992. Geological characteristics and tectonic setting of Proterozoic iron oxide (Cu-U-Au-REE) deposits. Precambr. Res. 58, 241–287.

Hitzman, M.W., 2000. Iron oxide-Cu-Au deposits: what, where, when, and why. In: In: Porter, T.M. (Ed.), Hydrothermal iron oxide copper-gold and related deposits a global perspective:, vol. 1. Australian Mineral Foundation, Adelaide, pp. 9–26.

Hou, T., Zhang, Z., Kusky, T., 2011. Gushan magnetite–apatite deposit in the Ningwu basin, Lower Yangtze River Valley, SE China: hydrothermal or Kiruna-type? Ore Geol. Rev. 43, 333–346.

Hu, H., Li, J., Lentz, D., Ren, Z., Zhao, X., Deng, X., Hall, D., 2014. Dissolution-reprecipitation process of magnetite from the Chengchao iron deposit: insights into ore genesis and implication for in situ chemical analysis of magnetite. Ore Geol. Rev. 57, 393–405.

Knipping, J.L., Bilenker, L.D., Simon, A.C., Reich, M., Barra, F., Deditius, A.P., Wälle, M., Heinrich, C.A., Holtz, F., Munizaga, R., 2015. Trace elements in magnetite from massive iron oxide-apatite deposits indicate a combined formation by igneous and magmatic-hydrothermal processes. Geochim. Cosmochim. Acta 171, 15–38.

Lepage, L.D., 2003. ILMAT: an excel worksheet for ilmenite–magnetite geothermometry and geobarometry. Comput. Geosci. 29 (5), 673–678.

Marks, M., Vennemann, T., Siebel, W., Markl, G., 2003. Quantification of magmatic and hydrothermal processes in a peralkaline syenite-alkali granite based on textures, phase equilibria, and stable and radiogenic isotopes. J. Petrol. 44 (7), 1247–1280.

Meinert, L.D., Dipple, G.M., Nicolescu, S., 2005. World Skarn Deposits. Economic Geology. 100th Anniversary Volume, pp. 299–336.

Monteiro, L.V.S., Xavier, R.P., Carvalho, E.R., Hitzman, M.H., Craig, A., Johnson, C.A., 2008. Spatial and temporal zoning of hydrothermal alteration and mineralization in the Sossego iron oxide–copper–gold deposit, Carajás Mineral Province, Brazil: paragenesis and stable isotope constraints. Miner. Deposita 43, 129–159.

Montreuil, J.F., Corriveau, L., Potter, E.G., De Toni1, A.F., 2016. On the relationship between alteration facies and metal endowment of iron oxide-alkali-altered systems, southern great bear magmatic zone (Canada). Econ. Geol. 111, 2139–2168.

Moreto, C.P.N., Monteiro, L.V.S., Xavier, R.P., Creaser, R.A., DuFrane, S.A., Tassinari,

C.C.G., Sato, K., Kemp, A.I.S., Amaral, W.S., 2015. Neoarchean and paleoproterozoic iron oxide-copper-gold events at the Sossego Deposit, Carajás Province, Brazil: Re-Os and U-Pb geochronological evidence. Econ. Geol. 110, 809–835.
Mücke, A., Cabral, A.R., 2005. Redox and nonredox reactions of magnetite and hematite in rocks. Chem. Erde 65, 271–278.
Mumin, A.H., Somarin, A.K., Jones, B., Corriveau, L., Ootes, L., Camier, J., 2010. The IOCG-Porphyry-Epithermal Continuum of Deposit Types in the Great Bear Magmatic Zone. Geological Association of Canada Short Course Notes, Northwest Territories, Canada, pp. 59–78 vol. 20.
Nadoll, P., Angerer, T., Mauk, J.L., French, D., Walshe, J., 2014. The chemistry of hydrothermal magnetite: a review. Ore Geol. Rev. 61, 1–32.
Nadoll, P., Mauk, J.L., Leveille, R.A., Koenig, A.E., 2015. Geochemistry of magnetite from porphyry Cu and skarn deposits in the southwestern United States. Miner. Deposita 50, 493–515.
Naslund, H.R., Henriquez, F., Nyström, J.O., Vivallo, W., Dobbs, F.M., 2002. Magmatic iron ores and associated mineralisation: examples from the chilean high andes and coastal cordillera. In: In: Porter, T.M. (Ed.), Hydrothermal Iron Oxide Copper-Gold and Related Deposits: A Global Perspective Vol. 2. PGC Publishing, Adelaide, pp. 207–226.
Navarro, M.S., Tonetto, E.M., Oliveira, E.P., 2017. Peixe Zircon: New Brazilian Reference Material for U-Pb Geochronology by LA-Sf-ICP-MS. Goldschmidt Abstract, Paris.
Nold, J.L., Davidson, P., Dudley, M.A., 2013. The pilot knob magnetite deposit in the Proterozoic St. Francois Mountains Terrane, southeast Missouri, USA: a magmatic and hydrothermal replacement iron deposit. Ore Geol. Rev. 53, 446–469.
Nold, J.L., Davidson, P., Dudley, M.A., 2014. The Southeast Missouri (USA) Proterozoic iron metallogenic province – types of deposits and genetic relationships to magnetite–apatite and iron oxide–copper–gold deposits. Ore Geol. Rev. 57, 154–171.
Padilha, A.L., Vitorello, Í., Pádua, M.B., Bologna, M.S., 2014. Electromagnetic constraints for subduction zones beneath the northwest Borborema province: evidence for Neoproterozoic island arc–continent collision in northeast Brazil. Geology 42 (1), 91–94.
Padilha, A.L., Vitorello, Í., Pádua, M.B., Fuck, R.A., 2017. Cryptic signatures of Neoproterozoic accretionary events in northeast Brazil imaged by magnetotellurics: implications for the assembly of West Gondwana. Tectonophysics 699, 164–177.
Paton, C., Woodhead, J.D., Hellstrom, J.C., Hergt, J.M., Greig, A., Maas, R., 2010. Improved laser ablation U-Pb zircon geochronology through robust downhole fractionation correction. Geochem. Geophys. Geosyst. 11, 1–36.
Parente, C.V., Verissimo, C.U.V., Botelho, N.F., Santos, T.J.S., Oliveira, C.G., Lira Junior, J.A., Martins, D.T., 2015. Depósitos de escarnitos mineralizados em ferro e cobre do arco magmático de Santa Quitéria, Ceará, Provincia Borborema do nordeste do Brasil. Braz. J. Geol. 45 (3), 359–382.
Passchier, C.W., Trouw, R.A.J., 2005. Microtectonics, 2ª ed. Springer, pp. 366.
Pollard, P.J., 2000. Evidence of a magmatic fluid and metal source for Fe-oxide Cu-Au mineralization. In: In: Porter, T.M. (Ed.), Hydrothermal Iron Oxide Copper-gold & Related Deposits: A Global Perspective, vol. 1. PGC Publishing, Adelaide, pp. 27–41.
Reich, M., Simon, A.C., Deditius, A., Barra, F., Chryssoulis, S., Lagas, G., Tardani, D., Knipping, J., Laura Bilenker, L., Sánchez-Alfaro, P., Roberts, M.P., Munizaga, R., 2016. Trace element signature of pyrite from the Los Colorados iron oxide-apatite (ioa) deposit, Chile: a missing link between andean ioa and iron oxide copper-gold systems? Econ. Geol. 111, 743–761.
Rhodes, A.L., Oreskes, N., Sheets, S., 1999. Geology and rare earth element geochemistry of magnetite deposits at El Laco, Chile. Soc. Econ. Geol. Spec. Publ. 7, 299–332.
dos Santos, T.J.S., Fetter, A.H., Neto, J.A.N., 2008. Comparisons between the northwestern Borborema Province, NE Brazil, and the southwestern Pharusian Dahomey Belt, SW Central Africa. Geol. Soc., London, Special Publ. 294 (1), 101–120. https://doi.org/10.1144/SP294.6.
Sillitoe, R.H., 2003. Iron oxide-copper-gold deposits: an Andean view. Miner. Deposita 38, 787–812.
Sillitoe, R.H., Burrows, D.R., 2002. Newfield evidence bearing on the origin of the El Laco magnetite deposit, northern Chile. Econ. Geol. 97, 1101–1109.
Skirrow, R.G., Bastrakov, E.N., Barovich, K., Fraser, G.L., Creaser, R.A., Fanning, C.M., Raymond, O.L., Davidson, G.J., 2007. Timing of iron oxide Cu-Au-(U) hydrothermal activity and Nd isotope constraints on metal sources in the Gawler craton, South Australia. Econ. Geol. 102, 1441–1470.
Tan, W., Liu, P., He, H., Wang, C.Y., Liang, X., 2016. Mineralogy and origin of exsolution in Ti-rich magnetite from different magmatic Fe-Ti oxide-bearing intrusions. Can. Mineral. 54, 539–553.
Tornos, F., Velasco, F., Hanchar, J.H., 2016. Iron-rich melts, magmatic magnetite, and superheated hydrothermal systems: The El Laco deposit, Chile. Geology. https://doi.org/10.1130/G37705.1.
Tornos, F., Hanchar, J.M., Velasco, F., Munizaga, R., Levresse G., 2017. The roots and tops of magnetite-apatite mineralization: Evolving magmatic-hydrothermal systems. In: 14th SGA Biennial Meeting Quebec City, Canada – August 20–23, 2017. In IOCG-IOA ore systems and their magmatic-hydrothermal continuum: A family reunion? vol. 3, pp. 831–834.
Treloar, P.J., Colley, H., 1996. Variations in F and C1 contents in apatites from magnetite-apatite ores in northern Chile, and their ore-genetic implications. Min. Mag. 60, 285–301.
Velasco, F., Tornos, F., Hanchar, J.M., 2016. Immiscible iron- and silica-rich melts and magnetite geochemistry at the El Laco volcano (northern Chile): evidence for a magmatic origin for the magnetite deposits. Ore Geol. Rev. 79, 346–366.
Veríssimo, C.U.V., Santos, R.V., Parente, C.V., Oliveira, C.G., Cavalcanti, J.A.D., Nogueira Neto, J.A., 2016. The Itataia phosphate-uranium deposit (Ceará, Brazil) new petrographic, geochemistry and isotope studies. J. South Am. Earth Sci. 70, 115–144.
Wiedenbeck, M., Allé, P., Corfu, F., Griffin, W.L., Meier, M., Oberli, F., Von, Q.A., Roddick, J.C., Spiegel, W., 1995. Three natural zircon standards for U-Th–Pb, Lu– Hf, trace element and REE analyses Geostand. Newsletter 19, 1–23.
Williams, P.J., Barton, M. D., Johnson, D.A., Fontbote L., Haller, A., Mark, G., Oliver, N.H. S., Marschik, R., 2005. Iron oxide copper gold deposits; geology, space-time distribution, and possible modes of origin: Economy Geology 100:371-406 (100th Ann Vol).
Xavier, R.P., Wiedenbeck, M., Trumbull, R.B., Dreher, A.M., Monteiro, L.V.S., Rhede, D., Araújo, C.E.G., Torresi, I., 2008. Tourmaline B-isotopes fingerprint marine evaporites as the source of high-salinity ore fluids in iron oxide copper-gold deposits, Carajás Mineral Province (Brazil). Geology 36 (9), 743–746.
Xavier, R.P., Monteiro, L. V. S., Rusk, B., Torresi, I., 2011. Comparing Iron Oxide Copper-Gold systems of the Carajás mineral province (Brazil) using apatite and magnetite trace elements: implications on genesis and exploration. 11th SGA Biennial Meeting Let's Talk Ore Deposits 26–29th September 2011 Antofagasta, Chile.
Zhao, X-F., Su, Z-K., Zeng, Li-Peng, 2017. Genetic models of IOCG and IOA deposits from China: Implications for ore genesis and their possible links. 14th SGA Biennial Meeting Quebec City, Canada – August 20–23, 2017: IOCG-IOA ore systems and their magmatic-hydrothermal continuum: A family reunion?, vol. 3, pp. 835–838.